

A 2MASS All-Sky View of the Sagittarius Dwarf Galaxy: IV. Modeling the Sagittarius Tidal Tails

David R. Law^{1,2}, Kathryn V. Johnston³, and Steven R. Majewski²

ABSTRACT

M giants recovered from the Two Micron All-Sky Survey (2MASS) have recently been used to map the position and velocity distributions of tidal debris from the Sagittarius (Sgr) dwarf spheroidal galaxy entirely around the Galaxy. We compare this data set to both test particle orbits and N-body simulations of satellite destruction run within a variety of rigid Milky Way potentials and find that the mass of the Milky Way within 50 kpc of its center should be $3.8 - 5.6 \times 10^{11} M_{\odot}$ in order for any Sgr orbit to simultaneously fit the velocity gradient in the Sgr trailing debris and the apocenter of the Sgr leading debris. Orbital pole precession of young debris and leading debris velocities in regions corresponding to older debris provide contradictory evidence in favor of oblate/prolate Galactic halo potentials respectively, leading us to conclude that the orbit of Sgr has evolved over the past few Gyr. In light of this discrepancy, we consider constraints from the younger portions of the debris alone within three models of the flattening of the Galactic potential ($q = 0.90/1.0/1.25$, i.e. oblate/spherical/prolate) in our further N-body simulations.

Based upon the velocity dispersion and width along the trailing tidal stream we estimate the current bound mass of Sgr to be $M_{\text{Sgr}} = 2 - 5 \times 10^8 M_{\odot}$ independant of the form of the Galactic potential; this corresponds to a range of mass to light ratios $(M/L)_{\text{Sgr}} = 14 - 36 (M/L)_{\odot}$ for the Sgr core. Models with masses in this range best fit the apocenter of leading Sgr tidal debris when they orbit with a radial period of roughly 0.85 Gyr and have periGalactica and apoGalactica of about 15 kpc and 60 kpc respectively. These distances will scale with the assumed distance to the Sgr dwarf and the assumed depth of the Galactic potential. The density distribution of debris along the orbit in these models is consistent with the M giant observations, and debris at all orbital phases where

¹California Institute of Technology, Department of Astronomy, MS 105-24, Pasadena, CA 91125 (dr-law@astro.caltech.edu)

²Dept. of Astronomy, University of Virginia, Charlottesville, VA 22903-0818 (srm4n@virginia.edu)

³Wesleyan University, Department of Astronomy, Middletown, CT (kvj@astro.wesleyan.edu)

M giants are obviously present is younger (i.e. was lost more recently from the satellite) than the typical age of a Sgr M giant star.

Subject headings: Sagittarius dwarf galaxy – Milky Way: halo – Milky Way: structure – Milky Way: dynamics – dark matter – Local Group

1. INTRODUCTION

The Sagittarius dwarf spheroidal galaxy (Sgr), discovered only a decade ago (Ibata, Gilmore, & Irwin 1994; Ibata, Gilmore, & Irwin 1995; Ibata et al. 1997), is the most compelling example of a satellite currently being cannibalized by the Milky Way. There have been numerous studies reporting the discovery of stars and star clusters plausibly associated with debris from this satellite, either trailing or leading it along its orbit (see Majewski et al. 2003 — hereafter “Paper I” — for a comprehensive summary). Using a study of faint, high-latitude carbon stars for which a significant overdensity was found to be aligned in angular position with the projection of Sgr’s orbit, Totten & Irwin (1998) were the first to present data that suggested that the tidal tails of the disrupting Sgr system extend a full 360° across the sky.

The conclusions of the carbon star study were recently dramatically verified using M giants selected from the 2MASS database (Paper I). Because Sgr is relatively metal-rich, M giant stars are prevalent in its debris stream, are far more common than carbon stars, and can be easily identified to distances of more than 50 kpc within the 2MASS database. Moreover, the large sample of M giants in the core of Sgr itself permits a much more reliable distance scale to be derived for these stars than is possible for the carbon stars. As a result, for the first time, primary leading and trailing tidal arms can clearly be traced using the 2MASS M giants, with the trailing tail spanning at least 150° across the Southern Galactic Hemisphere and the leading tail arcing up to create a rosette orbital loop in the Northern Galactic Hemisphere. Follow-up spectroscopy of Sgr-candidate stars has determined line-of-sight (i.e. “radial”) velocities for Sgr M giant stars throughout the trailing tail (Majewski et al. 2004a, hereafter “Paper II”), and work on stars in the leading trail is in progress (Majewski et al. 2004b, hereafter “Paper V”).

A number of groups have sought to model the Sgr — Milky Way interaction (e.g. Johnston, Spergel, & Hernquist 1995, Velazquez & White 1995, Ibata et al. 1997, Edelsohn & Elmegreen 1997, Johnston et al. 1999, Helmi & White 2001, Gómez-Flechoso, Fux, & Martinet 1999, Martínez-Delgado et al. 2004). The interaction of the Sgr dwarf spheroidal with the Milky Way offers a sensitive probe of the shape and strength of the Galactic

potential, and also provides a nearby laboratory for exploring the internal dynamics of satellite galaxies under the strong tidal influence of a parent system. Ibata & Lewis (1998) made an extensive series of simulations to match data available at the time. Among their models, model K6-a provides the closest match to the general morphology of the Sgr tidal tails as mapped by M giant stars selected from 2MASS. However, the 2MASS M giant work represents such a substantial increase in our knowledge of the phase-space distribution of Sgr debris that a new study of the system fully constrained by these data is warranted.

Recently, a controversy has begun to develop over the oblate/prolate nature of the Galactic halo as measured using Sgr tidal debris. Helmi (2004) has presented evidence in favor of a prolate ($q = 1.25$) halo using Sgr leading debris velocity trends, while in a companion paper (Johnston, Law, & Majewski 2004, hereafter “Paper III”) we have demonstrated that such prolate halos fail to reproduce the observed orbital pole precession of leading vs. trailing debris, for which oblate ($q = 0.90$) halos best reproduce observational data. In earlier studies, Ibata et al. (2001) and Martínez-Delgado et al. (2004) determined that values of $q \approx 1.0$ and $q = 0.85$ respectively best fit the available data. In this paper, we explore whether it is possible to resolve this conflict using a single-component (i.e. mass-follows-light) model for Sgr, traveling along a single orbit in a non-evolving potential. We present the results of numerical simulations to find the best fit to the measured positions and velocities of the M giants presented in Papers I, II, and V (preliminary results have been presented in Law et al. 2004) while allowing orbital, potential and Sgr internal parameters to vary. Our aim is to constrain the current mass and orbit of Sgr as tightly as possible as a precursor to further studies in which higher order effects (such as multi-component models for Sgr travelling along evolving orbits) are also accounted for.

In §2 we describe our simulation technique, and outline the properties of the observed tails that will be used to constrain the simulations. In §3.1 we use simple test particle simulations to examine what range of Galactic and orbital parameters could be consistent with Sgr debris. In §3.2 we use the results from full N-body simulations of satellite destruction along viable orbits in the chosen Galactic potentials to more tightly constrain the mass and orbit of Sgr. In §4 we compare our results to previous observational and numerical work and assess possible evolution of the Sgr orbit, and in §5 we summarize our conclusions.

2. METHOD

2.1. Baseline Galactic and Satellite Models

Our simulation technique closely follows that outlined in Johnston, Spergel, & Hernquist (1995). The Milky Way is represented by a smooth, rigid potential, and Sgr by a collection of 10^5 self-gravitating particles whose mutual interactions are calculated using a self-consistent field code (Hernquist & Ostriker 1992).

A three-component model is used for the Galactic potential and consists of a Miyamoto-Nagai (1975) disk, Hernquist spheroid, and a logarithmic halo:

$$\Phi_{\text{disk}} = -\alpha \frac{GM_{\text{disk}}}{\sqrt{R^2 + (a + \sqrt{z^2 + b^2})^2}}, \quad (1)$$

$$\Phi_{\text{sphere}} = -\frac{GM_{\text{sphere}}}{r + c}, \quad (2)$$

$$\Phi_{\text{halo}} = v_{\text{halo}}^2 \ln(R^2 + (z^2/q^2) + d^2). \quad (3)$$

Following Johnston et al. (1999), we take $M_{\text{disk}} = 1.0 \times 10^{11} M_{\odot}$, $M_{\text{sphere}} = 3.4 \times 10^{10} M_{\odot}$, $a = 6.5$ kpc, $b = 0.26$ kpc and $c = 0.7$ kpc. In §3.1 we investigate how different choices $\alpha = 0.25 - 1.0$, $q = 0.8 - 1.45$, $d = 1 - 20$ kpc and $v_{\text{circ},\odot} = 180 - 240$ km s $^{-1}$ (the circular speed at the Solar Circle — v_{halo} in Eqn. 3 was chosen to match $v_{\text{circ},\odot}$ for a given bulge and disk contribution and adopted d) affect our fit to the debris data.

Initially, the particles in our model of Sgr are distributed to generate a Plummer (1911) model

$$\Phi = -\frac{GM_{\text{Sgr},0}}{\sqrt{r^2 + r_0^2}}, \quad (4)$$

where $M_{\text{Sgr},0}$ is the initial mass of Sgr and r_0 is its scale length. These particles represent both the dark and light matter components of the satellite. We do not attempt to generate a more specific two-component model that matches Sgr's internal density and velocity distribution since both will evolve during the simulation. Rather, we explore to what extent Sgr's debris can constrain the present global characteristics of the satellite. These global characteristics can then be used in a more careful consideration of the core structure in future work when better data on the core are available.

2.2. Observational Constraints

In this paper we use the spherical, Sun-centered, Sgr-coordinate system¹ defined in Paper I, since this is the coordinate system in which satellite debris is observed and therefore can be compared to simulations most clearly. The zero-plane of the latitude coordinate B_{\odot} coincides with the best-fit great circle defined by Sgr debris, as seen from the Sun. The longitudinal coordinate Λ_{\odot} is zero in the direction of the Sgr core and increases along the Sgr trailing debris stream, i.e. away from the Galactic plane. Figure 1 shows a representative N-body simulation of the Sgr dwarf in Cartesian $X_{\text{Sgr,GC}}$, $Y_{\text{Sgr,GC}}$ coordinates (see Paper I for the definition of the Sgr,GC and Sgr, \odot coordinate systems), and illustrates the orientation of the spherical coordinate system with respect to the Galactic Plane. The colors of the simulated data used in this and other figures in this paper represent different debris “eras”, i.e. orbits (denoted as one apoGalacticon to the next apoGalacticon) on which the debris was stripped from the satellite. Yellow points represent debris stripped from the satellite since apoGalacticon about 0.5 Gyr ago, while magenta, cyan, and green points represent debris stripped from the dwarf 2, 3, and 4 orbits ago respectively. Note that while each color represents debris unbound from the satellite between two successive apoGalactic passages, the majority of debris of each color is released during the corresponding periGalactic passage. This color scheme allows us to discriminate readily between different wraps of tidal debris, and is also useful for determining the expected age of debris at any given point along the tidal stream.

The observed position and radial velocity data for Sgr M giants (Papers I, II, and V) provide strong constraints on the orbit of the Sgr dwarf. Most other Sgr detections around the sky fall within the M giant-traced tails (see Fig. 17 of Paper I); therefore we compare our models to the M giants alone because they offer the most consistent, wide-ranging map of Sgr debris, and at the same time encompass the previous detections. We compare our results to the recently announced SDSS detections (Newberg et al. 2003) in §4.1.

We define eleven observed properties that we adopt as constraints on our simulated Milky Way — Sgr system:

1. The model Sgr dwarf should be located at $(l, b) = (5.6^{\circ}, -14.2^{\circ})$ (Paper I).
2. The line-of-sight velocity² of the model dwarf should be $v_{\text{los,Sgr}} = 171 \text{ km s}^{-1}$ (Ibata et

¹C++ code to convert from standard Galactic coordinate systems to the Sgr longitudinal coordinate system can be obtained from the World Wide Web at <http://www.astro.virginia.edu/~srm4n/Sgr/>

²All velocities are given in the Galactic Standard of Rest (GSR) frame.

al. 1997).

3. Sgr debris should be aligned with the plane passing through the Sun having a pole $(l, b) = (273.8^\circ, -13.5^\circ)$ (Paper I).
4. The average heliocentric distance for Sgr leading debris at apoGalacticon (d_{avg}) in the Northern Galactic Hemisphere should be $42 \times (D_{\text{Sgr}}/24 \text{ kpc}) \text{ kpc}$, where D_{Sgr} is the assumed distance to Sgr (which sets the distance scale of the M giants and is taken to be 24 kpc in Paper I).
5. Radial velocities along the trailing stream from $\Lambda_\odot = 25^\circ - 140^\circ$ should match data presented in Paper II.
6. Radial velocities along the leading stream from $\Lambda_\odot = 230^\circ - 330^\circ$ should match data presented in Paper V.
7. The leading and trailing debris tails should define two distinct planes with poles offset from each other by ~ 10 degrees (Paper III).
8. The physical width of the trailing debris stream perpendicular to the orbital plane should be consistent with M giant observations (i.e. have a projected spatial dispersion $\sigma_{Z_{\text{Sgr}, \odot}} \approx 2.0 \text{ kpc}$).
9. The average radial velocity dispersion along the trailing stream from $\Lambda_\odot = 25^\circ - 90^\circ$ should match the dispersion found for M giants in Paper II ($\sigma_v = 10.0 \text{ km s}^{-1}$).
10. The model debris to which the M giant data are matched should be younger (i.e. have left Sgr more recently) than a typical Sgr M giant age (2-3 Gyr; see Paper I).
11. There should be a break in the surface density of trailing debris at $\Lambda_\odot \sim 20^\circ$, which has previously been interpreted (Mateo et al. 1998, Paper I) to correspond to the transition between debris lost on the current pericentric passage and that lost on the previous passage.

3. RESULTS

Table 1 outlines the Galactic and satellite parameters varied to produce a model that fits the constraints detailed above. Rather than run lengthy N-body simulations to randomly search for a global minimum in this degenerate, multi-dimensional parameter space (8 of which are allowed to vary), a more efficient, multi-step approach was taken to converge to the best fit to the observational data, relying on physical insight gained both from

analytical descriptions of debris dispersal (Tremaine 1993, Johnston 1998, Helmi & White 1999, Johnston, Sackett & Bullock 2001) and from previous modeling of Sgr by the authors (Johnston, Spergel, & Hernquist 1995, Johnston et al. 1999) and other groups (Velazquez & White 1995, Ibata et al. 1997, Edelsohn & Elmegreen 1997, Gómez-Flechoso, Fux, & Martinet 1999, Martínez-Delgado et al. 2004). These studies have found that while there is a systematic distance offset for leading/trailing debris inside/outside the orbit of the Sgr dwarf (a reflection of the debris moving to more/less tightly bound orbits — see Fig. 1) the line-of-sight velocity remains approximately aligned with that of the satellite’s orbit at all orbital phases. Hence in §3.1 below we are able to eliminate a wide range of orbits in a variety of Galactic potentials through test-particle integrations alone: We use constraint 4 as an upper limit on a possible orbit’s apocentric distance and examine how well the line-of-sight velocities along the orbit match the data in constraints 5 and 6. This technique allows us to find reasonable values for all of the free parameters listed in Table 1 except for Sgr’s current mass. In §3.2 we describe full-scale simulations of the destruction run for satellites of various masses along the orbits and in the potentials selected in §3.1.

3.1. Galactic Parameters

3.1.1. Varying initial conditions for test particle orbits

We assume Sgr’s current angular position, line-of-sight velocity and direction of proper motion to be fixed by constraints 1, 2 and 3 respectively, and adopt an amplitude for the motion of Sgr perpendicular to our line-of-sight (v_{\tan}) somewhere within ± 3 times the error bars on the Ibata et al. (2001) measurement of $280 \pm 20 \text{ km s}^{-1}$. The Sgr velocity and position relative to the Sun are then transformed to Galactocentric coordinates to provide initial conditions for the test particle orbits, assuming some values for the Solar distance from the Galactic center (R_{\odot}) and from Sgr (D_{Sgr}). (Note that changing D_{Sgr} from the assumed value of 24 kpc scales the distances to all of the Sgr M giants by the same fractional amount, since these distances are estimated from a color-apparent magnitude relation derived from M giants in Sgr’s core — Paper I). These orbits are then integrated backwards and forwards in time in the chosen Galactic potential (see §3.1.2) and the quality of fit of the orbital path to the M giant position and velocity data quantified (as described in §3.1.3).

3.1.2. Varying the Galactic potential — parameter and model choices

We anticipate that Sgr’s debris will tell us something about the contours of the gravitational potential in the region that its orbit explores ($\sim 10 - 50$ kpc). Hence we do not vary all parameters in equations (1) - (3), but instead hold the bulge component fixed and explore the effect of changing the contribution of the disk to the rotation curve through the parameter α , as well as the radial length scale, flattening, and overall depth of the halo potential respectively through the parameters d , q and $v_{\text{circ},\odot}$.

As a final check on the generality of our results, we repeat our experiments with the halo component replaced by models of the form proposed by Navarro, Frenk, & White (1996) — hereafter referred to as NFW models. In this case, the flattening is introduced in the density q_ρ , rather than potential contours, and the approximate form of the potential is adopted from Jing & Suto (2002). To explore a similar effective range in q and radial gradient as the logarithmic models, q_ρ and d (the length scale of the NFW potential) are chosen from a wider range than for their logarithmic counterparts — in particular, the range $5 < d < 100$ kpc was explored because this encompasses the range of scale lengths (of order tens of kpc) found for dark matter halos of similar mass-scale to the Milky Way in cosmological models of structure formation at the current epoch (e.g. Eke, Navarro, & Steinmetz 2001). The mass scale of the NFW potential is then constrained to match the adopted $v_{\text{circ},\odot}$.

3.1.3. Quantifying the fit of an orbit to the data.

A guideline for assessing the goodness of fit of an orbit to the positional data is that the maximum heliocentric distance observed for the leading debris (D_{debris} , constraint 4) must be systematically less than that of the orbit of the Sgr core, D_{max} — i.e. $D_{\text{max}}/D_{\text{debris}} > 1$. We can also find an upper limit to this ratio since we expect the size of this offset to scale as $\Delta R \propto R(M_{\text{Sgr}}/M_{\text{Gal}})^{1/3}$, where M_{Gal} is the mass of the Milky Way enclosed within the pericenter of the orbit (Johnston, Sackett, & Bullock 2001). For example, if we take this limit as $D_{\text{max}}/D_{\text{debris}} < 1.5$ then we might expect to cover all models with $M_{\text{Sgr}}/M_{\text{Gal}} < 0.125$ — i.e. Sgr masses up to 10% of the mass of the Milky Way. Since the internal dispersion measured for Sgr (11 km s $^{-1}$, Ibata, Gilmore, & Irwin 1995) suggests a mass far less than this we take $1 < D_{\text{max}}/D_{\text{debris}} < 1.5$ as a generous range for considering an orbit apogalacticon distance acceptable. Orbits with apogalactica outside this range are immediately rejected.

We next quantify the fit of orbits that are not already rejected to the trailing and leading

velocity data (constraints 5 and 6) through the parameters χ_{trail} and χ_{lead} :

$$\chi_{\text{A}}^2 = \frac{1}{N_{\text{A}}} \sum_{i=1}^{N_{\text{A}}} \frac{[v_{\text{Mgiant,A}}(\Lambda_{\odot}) - v_{\text{orb}}(\Lambda_{\odot})]_i^2}{\sigma_{\text{A}}^2} \quad (5)$$

where “A” represents the observed data set being considered (i.e. “lead” or “trail”), N_{A} is the number of M giants in the data set, $v_{\text{Mgiant}}(\Lambda_{\odot})$ is the velocity of an M giant at Λ_{\odot} and $v_{\text{orb}}(\Lambda_{\odot})$ is the velocity of the orbit at this Λ_{\odot} . The data compared to in the leading portion of the debris are selected by fitting a 3rd order polynomial to the full data set of velocities as a function of Λ_{\odot} in the range $230^{\circ} < \Lambda_{\odot} < 330^{\circ}$. Outliers from the main trend are thrown out using a 2.5σ iterative rejection technique until convergence is reached and the weight σ_{lead}^2 calculated as the dispersion of the velocities of this final set of N_{lead} stars about the best-fit polynomials. The process is then repeated for stars in the region $25^{\circ} < \Lambda_{\odot} < 140^{\circ}$ most sensitive to the trailing debris. The selected stars in both regions are plotted as black squares in Figure 2. Clearly, these data sets are not intended to represent a complete sample of Sgr stars, but rather as a guide to the general trends of velocities and dispersion in these regions.

We also express these quantities as a single parameter to measure the combined goodness-of-fit:

$$\chi = \sqrt{(\chi_{\text{trail}}^2 + \chi_{\text{lead}}^2)/2}. \quad (6)$$

Note that since test particle orbits only serve as an indication of where the debris should lie, we do not simply search for the parameters corresponding to the minima of these quantities: for example, we do not consider a difference of order $\Delta\chi < 0.1$ (corresponding to average systematic offsets $\sim 1 - 2 \text{ km s}^{-1}$ — very much less than the dispersion in the data) between the fit to two different orbits to be very significant. Rather, we use more extreme differences to rule out or favor broad regions of parameter space.

3.1.4. Combined constraints from leading and trailing velocity data

Although the velocity trends in the leading debris (constraint 6) appear to strongly favor Galactic models with prolate ($q > 1$) halo components (Helmi 2004), we have shown in Paper III that the direction of the precession of debris orbits (as measured by the offset in the poles of best-fit planes to leading and trailing debris — constraint 7) strongly favors models with oblate halos since prolate models induce precession in the *opposite* sense to that observed. Because no other adjustment to the potential can change the fundamental sense of precession in prolate *vs* oblate potentials, we restrict ourselves to asking whether

we can resolve this contradiction between the implications of constraint 6 and constraint 7 by revisiting the fit to the velocity and distance data alone over a much wider range of parameter space than has been considered previously. The aim is to examine whether there are any circumstances in which an orbit in an oblate potential can be found that can fit all the constraints at once.

Figure 3 plots the minimum values of χ_{trail} (solid lines), χ_{lead} (dotted lines) and χ (dashed lines) obtained as a function of q (left hand panel, logarithmic halo model) or q_ρ (right hand panel, NFW halo model) when all other parameters are allowed to vary freely within the ranges outlined in Table 1. The solid lines show that the trailing velocity data have a slight preference for models with oblate halos, although the difference $\Delta\chi_{\text{trail}} \sim 0.1$ between the minima for models with $q < 1$ and $q > 1$ is not sufficiently large that we can confidently rule out prolate models with test particle orbits alone, since it corresponds to a velocity offset much less than the dispersion in the data. In contrast, the dotted lines show that leading velocity data strongly prefer prolate halo models, to such an extent that this preference dominates the combined χ (dashed lines). These results are the same for the logarithmic and NFW models.

Overall, we conclude that we cannot find a single orbit in a static potential model that simultaneously fits the velocity data in the trailing data together with the sense of precession suggested by the offset of the planes of the leading *vs* trailing data.

3.1.5. Constraints from trailing velocity data alone

The exciting implication of the conclusion of the previous section — that no *single* orbit and/or potential can fit all the data — is that some evolution of Sgr’s orbit has occurred over the time since debris in the leading portion of the streamer, furthest in Λ_\odot from Sgr, was released. We discuss some possible culprits for this orbital evolution in §4.3, but defer a detailed investigation of these effects for future work. For the remainder of this study, we narrow our present analysis to concentrate on the younger portions of the debris, lost within the last 1-2 orbits, where (1) the effect of orbit evolution is negligible, (2) the modelling can be achieved with the fewest free parameters, and (3) the interpretation of the data is less ambiguous. The goal is to ask what the younger debris alone can tell us about the Galactic potential and Sgr’s current mass and orbit. These results can subsequently be used as starting points for studies that use the older debris to examine higher order effects such as orbital evolution, evolution of the potential, and/or multi-component models for Sgr.

We expect debris in the trailing streamer in the range explored by the velocity data to

be roughly the same age as that in the early parts of the leading streamer to about the first apocenter (as demonstrated by Helmi 2004, and see also §3.2 below). In these regions, the velocity data can be similarly fit by both oblate and prolate potentials (as demonstrated by the solid lines in Figure 3), and there is no significant offset in the orbital poles between the leading and trailing components. Hence, we now drop constraints 6 and 7 on our models since these were derived from regions where orbit evolution could be significant. We continue our discussion of test-particle constraints on the Galactic potential and our position relative to the Galactic center and Sgr using the condition $1 < D_{\text{max}}/D_{\text{debris}} < 1.5$ and examining χ_{trail} alone.

In order to sort through our large parameter space, we first look at parameters that do not appear to be strongly constrained by the data and fix reasonable values for those (see discussion in A. and B. below) before going on to look at preferred ranges for the remaining parameters (in C.).

A. Implications for distance scales

In the upper left hand panels of Figures 4 (for logarithmic halo experiments) and 5 (for NFW halo experiments) we project results in our 7-dimensional parameter space onto the 2-dimensions of D_{Sgr} and D_{Sgr}/R_{\odot} by plotting the minimum value of χ_{trail} at each point in this plane when all other parameters are allowed to vary freely. The plots reveals a preference for larger values of the ratio D_{Sgr}/R_{\odot} , with the absolute scale (as set by D_{Sgr}) being arbitrary. For consistency with the distance scales adopted earlier in Paper I we choose to take $D_{\text{Sgr}} = 24$ kpc (which also lies within the 2σ error bars of the recent measurement by Monaco et al. 2004) and set $R_{\odot} = 7$ kpc. So long as $D_{\text{Sgr}}/R_{\odot} \sim 3.4$ we expect all subsequent results involving distances (e.g. scale-length of the halo d , or predicted distances to debris) can be scaled by whatever value D_{Sgr} is assumed in a given study.

B. Implications for the Galactic rotation curve

With $D_{\text{Sgr}} = 24$ kpc and $R_{\odot} = 7$ kpc fixed, the upper right hand panels of Figures 4 and 5 project the remaining five-dimensions of parameter space onto the $v_{\text{circ},\odot} - \alpha$ plane. For high enough $v_{\text{circ},\odot}$ there is no preference for a particular α , but models with lower $v_{\text{circ},\odot}$ are inconsistent with heavier Galactic disks (i.e. higher α).

Figure 6 offers some clue as to why this is the case by plotting rotation curves for only those potentials in which orbits with $\chi_{\text{trail}} < 1.1$ could be found. These are very flat out to large radii for all models, with circular velocities at 50 kpc in the range $180\text{--}220$ km s $^{-1}$ (which corresponds to enclosed masses for the Milky Way at these radii of $3.8\text{--}5.6 \times 10^{11} M_{\odot}$

— in effect, Sgr debris velocities are now providing additional evidence for the existence of a dark matter halo to the Milky Way). If enough of the contribution $v_{\text{circ},\odot}$ is provided by the disk, then the remaining halo component is simply not massive enough to support such an extended flat rotation curve. (Larger mass halos could be built by allowing d an even wider range, but these models would [i] have rising rotation curves at the Solar Circle; and [ii] be inconsistent with scale lengths measured for Milky Way-sized dark matter halos formed in cosmological models of structure formation — see Eke, Navarro & Steinmetz, 2001).

Since no values of α and $v_{\text{circ},\odot}$ are at this point clearly preferred, we adopt $\alpha = 1.0$ and $v_{\text{circ},\odot} = 220 \text{ km s}^{-1}$.

C. Summary of parameter choices and conclusions

The colored lines in the lower panels of Figures 4 and 5 demonstrate that, with $R_\odot = 7 \text{ kpc}$, $D_{\text{Sgr}} = 24 \text{ kpc}$, $\alpha = 1$ and $v_{\text{circ},\odot} = 220 \text{ km s}^{-1}$ fixed, particular values for d (which determines the radial gradient of the potential and hence the shape of the rotation curve) and v_{tan} (which determines the scale of the orbit within this potential) are quite strongly preferred, with only a mild dependence on q . Hence we perform full N-body simulations in potentials with logarithmic halos in which $q = 0.9/1.0/1.25$, $d = 13/12/11 \text{ kpc}$ (from the minima in the lower left hand panels) and v_{tan} in the range $\pm 20 \text{ km s}^{-1}$ around $280/270/254 \text{ km s}^{-1}$. All three values, $q = 0.9/1.0/1.25$, are considered since all represent equally viable fits to the younger debris.

Clearly, our choices are not unique. The black curves in the lower panels of Figures 4 and 5 outline where the colored lines would fall if all other parameter choices were the same but $v_{\text{circ},\odot} = 240 \text{ km s}^{-1}$ (dashed lines) or $\alpha = 0.5$ (dotted lines). In both cases, the scale-length changes significantly in order to maintain the necessary flatness of the rotation curve, and v_{tan} is similarly affected.

In addition, our decision to use logarithmic halos rather than NFW halos is arbitrary, since Figures 4 and 5 reveal no preference for either form of the potential, but rather more generally indicate that any model that generates a flat rotation curve out to 50 kpc will suffice. We anticipate that data exploring even larger distances from the Galactic center will be able to address whether an NFW (with a falling rotation curve in this region) or logarithmic potential is more appropriate.

Despite these multiple minima in parameter space, we are able to reach some general conclusions at this point: (i) Sgr debris data prefers models with large values of D_{Sgr}/R_\odot and flat rotation curves out to 50 kpc, and (ii) with all other parameters fixed, Sgr orbits in prolate halos will have systematically lower v_{tan} than in spherical or oblate halos. These

conclusions offer a tantalizing glimpse of how Sgr debris might be used to map out the Galactic potential on large scales once parameters such as R_\odot and v_{\tan} are known with more certainty.

3.2. Sagittarius’ Properties

Using the Galactic parameters determined in §3.1 above, we now perform fully self-consistent N-body simulations to refine the estimates obtained in §3.1 of Sgr’s orbital velocity and to determine the mass of the dwarf. These simulations follow the evolution of satellites with a range of initial masses and physical scales (varied through the parameters $M_{\text{Sgr},0}$ and r_0 in Equation [4]) along a small range of plausible orbits within the three models of the Galactic potential ($q = 0.9/1.0/1.25$)³ discussed in §3.1.5C.

In §3.2.1 we find the mass of Sgr (independent of r_0) that best fits constraints 8 and 9 in each of these three models of the Galactic potential, and demonstrate that this best-fit mass is common to all three cases. Fixing the satellite mass to this best-fit value, we refine our estimate for Sgr’s tangential velocity using constraints 4 and 5 in §3.2.2 and summarize the properties of our best-fit models in §3.2.3.

3.2.1. Constraining the Mass of the Sgr Dwarf

While we do not attempt to model the Sgr core in detail, we are nonetheless able to constrain its current total mass under the assumptions that the dwarf is roughly spherical and non-rotating. Motivated by previous work (e.g., Johnston, Hernquist, & Bolte 1996, Johnston 1998) we expect that debris width (constraint 8) and velocity dispersion (constraint 9) at a given orbital phase primarily reflect the mass within the tidal radius of the satellite on the orbit immediately prior to that debris becoming unbound, and that they do not depend strongly on the internal structure of the satellite (in our case parameterized by the scale length of the initial Plummer model). For the same reasons, we do not expect that our results are strongly sensitive to the particle distribution we have adopted. We do expect the internal orbital distribution will independently affect debris morphology, but do not address that issue in this paper.

To compare the simulations to the data constraints, we calculate the average radial

³We adopt the convention of stating values derived in each of these potentials for oblate/spherical/prolate cases, respectively.

velocity dispersion σ_v and the average dispersion of distances perpendicular to the Sgr plane $\sigma_{Z_{\text{Sgr},\odot}}$ in the trailing tail for M giant data and our numerical simulations. We do not consider leading debris in obtaining our mass estimates since only our prolate halo model successfully matches the *bulk* trend of leading debris, while all three halo models reproduce the trailing debris trend. σ_v is calculated in the range $\Lambda_\odot = 25^\circ - 90^\circ$ for consistency with the velocity dispersion analysis presented in Paper II, while $\sigma_{Z_{\text{Sgr},\odot}}$ is calculated in the range $\Lambda_\odot = 60^\circ - 120^\circ$ since this range of debris longitudes is one for which all Sgr stars in the sample⁴ are at a similar distance d_* from the Sun (this minimizes artificial width inflation on the sky due to differential distance errors) and is also in a region of the Galaxy where sample contamination by Milky Way disk stars is negligible.

Figure 7 plots the calculated velocity dispersion (left-hand panels) and width (right-hand panels) as functions of simulated bound satellite mass for choices of $q = 0.9$ (lower panels), 1.0 (middle panels), and 1.25 (upper panels). In all panels the M giant dispersion/width is plotted as a solid line with $1-\sigma$ error bars indicated by the hatched regions, while the points in all panels indicate N-body simulation results (incorporating a 17% artificial distance scatter to simulate the photometric distance errors given in Paper I) for model satellites evolved along the orbits found earlier in §3.1.5C for a variety of choices of initial satellite mass ($M_{\text{Sgr},0} = 10^7 M_\odot - 5 \times 10^9 M_\odot$) and physical scale ($r_0 = 0.2 \text{ kpc} - 1.5 \text{ kpc}$).

Clearly, similar values of M_{Sgr} are preferred for models in oblate, spherical, and prolate Galactic potentials alike. To quantify more precisely the range of acceptable masses indicated by Figure 7 we fit the data points in each panel with a third-order polynomial with $2.5-\sigma$ rejection criteria iterated to convergence and extrapolate from the resulting power-series coefficients the mass range whose σ_v and $\sigma_{Z_{\text{Sgr},\odot}}$ lie within the $1-\sigma$ uncertainty range around the M-giant measurements. These results, presented in tabular form in Table 2, indicate that in all models of the Galactic potential considered the present bound mass of the Sgr dwarf should not be very different from $M_{\text{Sgr}} = 2 - 5 \times 10^8 M_\odot$ if the model dwarf is to successfully reproduce the M giant observations.

3.2.2. Constraining the Velocity of the Sgr Dwarf

We now fix the initial mass and scale of the model dwarf such that the present-day dwarf has a bound mass in the range found above in §3.2.1, and endeavor to refine our orbits using the single remaining free parameter v_{\tan} . We explore a range of values $\pm 20 \text{ km s}^{-1}$ around

⁴This sample is drawn directly from the 2MASS database with the selection criteria $E(B - V) < 0.555$, $1.0 < J - K < 1.1$, $|Z_{\text{Sgr},\odot}| < 5$, $Z_{\text{GC}} < 0$, and $13 \text{ kpc} < d_* < 40 \text{ kpc}$.

the values $v_{\tan} = 280/270/254 \text{ km s}^{-1}$ chosen from test-particle orbits previously in §3.1.5C. Note that it is not possible to fix the final bound mass of the satellite in these simulations, since the change in the orbital path produced by varying v_{\tan} will naturally affect the mass-loss history of the model dwarf. However, as demonstrated by Figure 7 (filled triangles) these small variations in v_{\tan} have only a minor effect on the final mass of the model dwarf.

Returning to constraint 4 on the average apoGalacticon distance of leading debris, the average distance of observed leading Sgr debris (d_{avg}) is calculated from the 2MASS database by averaging over the distances of all stars in the range $\Lambda_{\odot} = 280^\circ - 320^\circ$ with heliocentric distances $30 \text{ kpc} < d_* < 60 \text{ kpc}$ and subject to the restrictions $E(B-V) < 0.555$, $1.0 < J - K < 1.1$, $|Z_{\text{Sgr},\odot}| < 5 \text{ kpc}$, $Z_{\text{GC}} > 10 \text{ kpc}$ (this combination of restrictions was chosen to separate Sgr leading arm stars most clearly from the underlying disk population). Figure 8 plots the average apoGalacticon distance of the M giants as a solid line with $1-\sigma$ error bars indicated by the hatched region, along with the values calculated from the simulated data (again incorporating a 17% distance uncertainty) for the simulations with fixed initial mass and physical scale but varying v_{\tan} (filled triangles). Simulations with a range of initial masses and physical scales whose present bound mass falls within the acceptable range found in the previous section are also plotted (filled squares and crosses): These points are difficult to distinguish since M_{Sgr} and r_0 are not the primary factors governing the behavior of d_{avg} , demonstrating the minor variation in d_{avg} permitted by the remaining uncertainty in satellite mass. While Figure 8 shows a strong correlation between leading debris distance and orbital velocity however, the relatively large uncertainty in the M giant debris distance allows us only to place constraints on the dwarf velocity to within about $\pm 20 \text{ km s}^{-1}$.

A more compelling velocity constraint can be obtained by again using constraint 5, that the trailing arm velocities match those observed for M giants. We calculate the average offset of the centroid of simulated trailing debris velocities⁵ from the M giant centroid and plot these offsets as a function of the tangential velocity of the dwarf in Figure 9. Well defined minima corresponding to the best fits to the velocity data are obtained for specific velocities in each choice of the Galactic potential, and are fairly insensitive to the remaining uncertainties in satellite mass (filled squares and crosses). We therefore conclude that the best choices of tangential velocity for the model dwarf are $v_{\tan} = 275-280/265-270/250-260 \text{ km s}^{-1}$ (note that, in this case, the best-fit test particle orbits obtained in §3.1.5C actually picked out the best orbits for the N-body simulations). Although each of these estimates are reasonably consistent with the observed value $v_{\tan} \approx v_b = 280 \pm 20 \text{ km s}^{-1}$ measured by Ibata et al. (2001), it is interesting to note that the Ibata et al. (2001) measurement

⁵In the interests of consistency with previous analyses in Paper II, we again use the range $\Lambda_{\odot} = 25^\circ - 90^\circ$.

appears to slightly favor oblate models of the Galactic halo over prolate models at the $1-\sigma$ level for our current choice of $v_{\text{circ},\odot} = 220 \text{ km s}^{-1}$. Note, however, that a higher value of $v_{\text{circ},\odot}$ will systematically shift these estimates of v_{tan} to higher velocities (see Figs. 4 & 5, dashed line in lower right-hand panels), resulting in better agreement of estimates of v_{tan} in prolate halos with the Ibata et al. (2001) measurement.

3.2.3. Our best-fit model

Based upon Figures 7, 8, and 9, simulations with $M_{\text{Sgr}} = 2.6\text{-}5.0/2.5\text{-}5.3/2.5\text{-}5.5 \times 10^8 M_{\odot}$ and $v_{\text{tan}} = 275\text{-}280/265\text{-}270/255\text{-}260 \text{ km s}^{-1}$ best fit our constraints, and these models are hereafter referred to as our “best-fit models”⁶. Although the uncertainty in the Galactic potential gives rise to uncertainties in v_{tan} considerably greater than the ranges given here, within a given potential v_{tan} can be constrained to within about $\pm 5 \text{ km s}^{-1}$. Our best-fit models have a maximum extent of bound material $r_{\text{bound}} \sim 500'$ along the semi-major axis, within which we calculate a luminosity for Sgr of $L_{\text{Sgr}} = 1.4 \times 10^7 L_{\odot}$ using data presented in Paper I. The mass-to-light ratio of Sgr in these models should therefore be $M_{\text{Sgr}}/L_{\text{Sgr}} = 19\text{-}36/18\text{-}38/18\text{-}39 M_{\odot}/L_{\odot}$. While the 500' maximum extent for bound material is somewhat dependent on the adopted internal structure of the satellite, it is on the order of the true tidal radius previously pointed out (§4.3.3 of Paper I) as required to avoid Sgr having a quite extraordinary (and unlikely) bound mass, and is also of order the observed *minor* axis dimension (i.e., 0.35 times that of the 1801' major axis radius) of the limiting radius of the fitted King profile to the central satellite.

These orbits have periods of 0.85/0.88/0.87 Gyr with periGalactica and apoGalactica of 10-16/14/14-19 kpc and 56-58/59/56-59 kpc respectively⁷, and a present space velocity $(U, V, W)^8 = (238, -42, 222)/(235, -40, 213)/(231, -37, 198) \text{ km s}^{-1}$, corresponding to $(\Pi, \Theta, Z) = (230, 75, 222)/(227, 73, 213)/(224, 69, 197) \text{ km s}^{-1}$ and $(v_r, v_b, v_l) = (171, 272, -65)/(171, 263, -63)/(171, 247, -59) \text{ km s}^{-1}$ with respect to the Galactic standard of rest. These velocities will scale roughly with the assumed value of $v_{\text{circ},\odot}$, although will also depend

⁶Complete data files of model Sgr debris from these best-fit models are provided on the web at <http://www.astro.virginia.edu/~srm4n/Sgr/> to aid future comparisons of these models with new observations and new disruption models.

⁷Note that *ranges* are given for non-spherical potentials since for such non-spherically symmetric potentials the apoGalacticon and periGalacticon distances are dependant upon the polar angle of the satellite, and hence these distances may vary slightly from orbit to orbit.

⁸We adopt a right-handed Galactic Cartesian coordinate system with origin at the Galactic Center.

systematically upon q , d , and α .

Figure 10 plots simulated Sgr debris for our best-fit models along with the M giant distance and velocity data from Papers I, II and V, and demonstrates visually that our models generally fit the M giant observations well. The M giant data is clearly traced by debris released during the last two pericentric passages of the model dwarf (yellow and magenta points) and possibly by debris released three pericentric passage ago (cyan points), although there appear to be far fewer M giants corresponding to cyan points than magenta or yellow. This corresponds to M giants becoming unbound from the Sgr dwarf over the last 1.5 - 2.5 Gyr — consistent with constraint 10, that the debris age be younger than the typical age of an M giant star. Note, however, that as predicted by the orbits in §3.1 models in oblate and spherical halo potentials fail to fit the leading velocity trend (particularly for cyan points), while the model orbiting in a prolate potential both reproduces this velocity trend and provides a more convincing fit to the apparent trend of M giant distances at $\Lambda_\odot \sim 220^\circ - 260^\circ$. Note also the presence of cyan and green debris within a few kpc of the Sun over a wide range of Λ_\odot for oblate and spherical halo models - this is a consequence of the leading streamer diving almost directly through the Solar Neighborhood in these two models. Conclusive proof of the presence or absence of Sgr debris around the Sun would provide a significant additional constraint on the models.

The density of stars in the trailing stream for the best-fit models is plotted as a function of Λ_\odot in Figure 11, and is similar in structure to the density of the M giant stream (constraint 11, plotted in Fig. 13 of Paper I), with a break in the slope of the density profile around $\Lambda_\odot = 20$ degrees and a relatively constant density thereafter (we only consider this first break in the observed density profile since we expect this to depend primarily upon satellite mass). The details of the run of density along the trailing streamer will depend on the internal light distribution of the satellite. However, since we consider only single-component models in this paper, we omit further consideration of the density profile and internal structure of the dwarf at this time.

4. DISCUSSION

4.1. Comparisons with Previous Data

As noted in §2.2, most other Sgr detections around the sky fall within the M giant-traced tails (see Fig. 17 of Paper I), so that our best-fit models also provide a good match to these other data. In this section, we compare our predictions for older Sgr debris (green points) not traced by the M giants with observations of older tracers.

In Figure 12, carbon star data⁹ (open boxes) are plotted for comparison with our best-fit Sgr models (colored points). While some of the carbon stars appear consistent with both M giant and simulated debris, many others have distances and velocities that differ substantially from the M giant and model distributions, and attempts to fit simulation models to these carbon stars will likely produce results that differ noticeably from our own best-fit models and the M giant data. Although some of this discrepancy could be due to the uncertain distance scale for the carbon stars (see §8.3 of Paper I), it is also possible that these stars could trace debris older than the ~ 2.5 Gyr old M giant stream, since carbon stars can have larger ages (5 - 6 Gyr) than M giants.

The open triangles near $\Lambda_\odot \sim 300^\circ$ in Figure 12 represent data for a set of metal-poor, K-giant stars first pointed out by Kundu et al. (2002). Using semi-analytical modeling, Kundu et al. (2002) proposed that these stars represent debris stripped from Sgr three pericentric passages ago (corresponding to cyan-colored points in our model). Indeed, our model suggests that these points may plausibly be fit by cyan or green debris (i.e. debris from 3 - 4 pericentric passages ago) in the $q = 0.90$ leading streamer that is currently raining down from the North Galactic Pole onto the Solar Neighborhood, although the interpretation of these data is uncertain in models where $q = 1.0$ or 1.25 .

We also note an interesting comparison with possible Sgr red clump stars detected in a pencil-beam survey by Majewski et al. (1999) at $(l, b) = (11^\circ, -40^\circ)$, and for which the radial velocity data are plotted in Figure 12 (top panel, solid triangles). These stars at $\Lambda_\odot = 27^\circ$ exhibit a range of line-of-sight velocities from 0 to 150 km s^{-1} , which closely matches the predicted range of velocities of simulated leading tidal debris wrapped almost 360° in orbital longitude from the Sgr dwarf (cyan and green points) for simulations where $q = 1.0$ or 1.25 . The degree of this agreement is highly sensitive to the mass of the model satellite: Simulations with present mass $M_{\text{Sgr}} = 5 \times 10^8 M_\odot$ predict a larger dispersion in velocities than observed by Majewski et al., while simulations with mass $M_{\text{Sgr}} = 2 \times 10^8 M_\odot$ predict a smaller dispersion than observed. It is tempting therefore to point to these data as further evidence in favor of the satellite mass estimates determined earlier in §3.2.1 However, the distance to these stars is measured to be roughly 20 kpc (Majewski et al. 1999) — about half that of the cyan - green leading debris whose velocities they reproduce so well — and therefore, while they are interesting to compare to model data, their true origin and interpretation remains unclear.

Recently, the discovery of an overdensity of A-colored stars in the Sloan Digital Sky

⁹Carbon stars have been selected from Totten & Irwin (1998) subject to the requirement that both distance and velocity data have been measured, and also subject to the photometric criteria employed by Ibata et al. (2001) that $11 < R < 17$ and $B_J - R > 2.5$.

Survey with apparent magnitude $g_0 \sim 20.3$ at $\Lambda_\odot = 187^\circ - 212^\circ$ degrees and within 15 kpc of Sgr’s nominal orbital plane was announced (Newberg et al. 2003). These authors estimate an average heliocentric distance of 83 kpc to these stars, but note that other detections in directions which overlap the M giant stream suggest that their adopted distance scale is 12.5% larger than that used to calibrate the M giants in Paper I. The open circle in Figure 12 (left-hand panels) plot the average of their data, with the distance rescaled to 73 kpc so that the M giant and SDSS distance scales match. Figure 12 suggests that it is plausible to identify the SDSS detection with debris of age $\sim 1.5 - 2.5$ Gyr (i.e. cyan-colored points) in the trailing Sgr stream, although future radial velocity measurements could help determine whether this identification is correct or if the Newberg et al. feature is instead a part of some older, more distant section of the stream or even halo substructure unrelated to Sgr. Newberg et al. (2003) also note a hint of precession in the Sgr stream by comparing their detections of leading and trailing debris closer to Sgr’s core, in agreement with our own results presented in Paper III. Unfortunately, the angular extent of the 83 kpc debris has not yet been mapped accurately enough to pinpoint the angular position of the centroid of the debris; such a measurement could in the future provide a strong constraint on the flattening of the Galactic potential.

4.2. Comparisons with Previous Sgr Simulations

Previous attempts to model the orbit and disruption history of the Sgr dwarf (e.g. Velazquez & White 1995, Johnston, Hernquist & Bolte 1996, Ibata et al. 1997, Edelsohn & Elmegreen 1997, Ibata & Lewis 1998, Gómez-Flechoso, Fux & Martinet 1999, Johnston et al. 1999, Helmi & White 2001, Ibata et al. 2001, Martínez-Delgado et al. 2004) have made considerable progress in constraining models of the dwarf using only the previously available pencil-beam detections of satellite debris. In this paper we have presented the first model based upon a complete all-sky view of the satellite’s tidal streams, and in this section we review and compare some of the predictions of these earlier models to those of our own best-fit models.

We first consider those results for which the majority of simulations by different groups have generally converged. Almost all simulations agree that the radial period of the Sgr dwarf should be about 3/4 Gyr: In this work we find a period for our best-fit models of 0.85/0.88/0.87 Gyr, in reasonable agreement with previous estimates of 0.76 Gyr (Velazquez & White 1995, Ibata et al. 1997), 0.7 Gyr (Ibata & Lewis 1998), 0.55-0.75 Gyr (Johnston et al. 1999), 0.85 Gyr (Helmi & White 2001), and 0.74 Gyr (Martínez-Delgado et al. 2004). There is a little more spread in the estimates proposed by different groups for the

periGalacticon and apoGalacticon distances of the dwarf’s orbit: Previous estimates include (respectively) 10 kpc and 52 kpc (Velazquez & White 1995), 15 kpc and 60 kpc (Ibata & Lewis 1998), 15 kpc and 70 kpc (Gómez-Flechoso, Fux & Martinet 1999), 13 kpc and 41 kpc (Johnston et al. 1999), 16 kpc and 60 kpc (Ibata et al. 2001), and 12 kpc and 60 kpc (Martínez-Delgado et al. 2004). With the 2MASS database it is possible to measure the apoGalacticon of leading tidal debris directly, and we match this constraint best by using models for Sgr that have orbits with periGalacticon and apoGalacticon distances of 10-16/14-14-19 kpc and 56-58/59/56-59 kpc respectively. We note, however, that the distance scale assumed for the M giants in Paper I is not yet secure, and that the estimated size of Sgr’s orbit may scale accordingly.

Among those areas in which common values among the disruption models presented by various groups have not yet been found, perhaps foremost is the V component of the Galactic (U, V, W) velocity of the Sgr dwarf. Some simulations (e.g., Ibata et al. 1997) have simply set $V = 0 \text{ km s}^{-1}$ (thereby assuming a polar orbit) since this component was so poorly known. Now that we have an accurate measurement of Sgr’s orbital pole (Paper I), we are able to predict the direction of its motion more precisely. Based on our best-fit model, we predict that the proper motion of the Sgr dwarf should be $\mu_l \cos(b) = -2.59/-2.57/-2.54 \text{ mas yr}^{-1}$ and $\mu_b = 2.26/2.18/2.05 \text{ mas yr}^{-1}$ in the Solar rest frame¹⁰. The direction of this proper motion prediction ($\mu_b/\mu_l \cos(b) = 0.87/0.85/0.81$) is expected to be fairly robust within potentials with each choice of q . However, the amplitude of the proper motion will depend on the exact form of the Galactic potential, and hence should be revised once other fundamental Galactic parameters such as R_\odot and $v_{\text{circ},\odot}$ are known more precisely. Conversely, as more accurate measurements of Sgr’s proper motion become available it will be possible to refine constraints on the Galactic rotation curve.

A second area of debate concerns the present bound mass of the Sgr dwarf, for which estimates range from $M_{\text{Sgr}} = 7.0 \times 10^6 M_\odot$ (Martínez-Delgado et al. 2004) to $M_{\text{Sgr}} = 1.0 \times 10^9 M_\odot$ (Ibata et al. 1997). Helmi & White (2001) find an intermediate value for a purely stellar satellite model with initial mass $M_{\text{Sgr},0} \approx 5.0 \times 10^8 M_\odot$. As demonstrated in §3.2.1, we find that a range of final masses $M_{\text{Sgr}} = 2 - 5 \times 10^8 M_\odot$ yield tidal tails whose thickness and velocity dispersion are consistent with M giant measurements in oblate, spherical, and prolate models of the Galactic potential. Using Figure 7 we conclusively rule out models with a mass far outside this range (such as that of Martínez-Delgado et al. 2004), since models with very high or low masses will not be able to produce tidal tails with the observed thickness and dispersion. Visual inspection of the figures in Martínez-Delgado et al. (2004)

¹⁰We adopt a solar peculiar velocity of $(U, V, W) = (9, 12, 7) \text{ km s}^{-1}$ relative to the LSR, for which we adopt a rotation velocity of 220 km s^{-1} (§3.1.5B).

appears to contradict this statement. However, these authors’ simulation embeds the model satellite in a 40,000 particle live halo, which is probably responsible for the width of the debris stream: Earlier work (Johnston, Spergel & Haydn 2002) has found that significant heating of a Sgr-like debris stream can occur in a simulation using a live halo, even in a halo model realized with 10^6 particles.

As another consequence of the smaller satellite mass used in their model, Martínez-Delgado et al. (2004) predict leading debris at $(\alpha, \delta) = (210^\circ, 0^\circ)$ (corresponding to $\Lambda_\odot = 284^\circ$) to be composed of stars which have been unbound from the satellite for 5 Gyr or more (since debris from lower-mass satellites takes longer to spread along the orbit), in contrast to the roughly 2 Gyr found by our own analysis. As demonstrated in Figure 10, the Sgr M giants — which have an estimated age of 2-3 Gyr — are visible to at least this point in the leading tidal stream. As Martínez-Delgado et al. (2004) point out (and we discuss in Paper I), stellar populations formed in the densest central regions of the satellite should not be immediately reflected in the tidal streams, and it will take some time for these stars to be present in any quantity in the outer regions of the satellite. Hence, it is unlikely that the M giant population became mixed into the outer regions of Sgr within a small fraction of a Gyr, and we consider the mean age estimate of 5 Gyr for this section of the tidal stream to be too high.

4.3. Evolution of Sgr’s Orbit

In Paper III we showed that only Galactic potentials with oblate halos could reproduce the precession of the orbital plane apparent in the leading *vs* trailing data sets. In contrast, Helmi (2004) demonstrated that only Galactic potentials with prolate halos could reproduce the velocity trends in the leading debris. In this paper (§3.1) we explore a much wider variety of Galactic potentials than has been considered previously but fail to find a single orbit that can fit both the velocity trends and sense of precession. Our conclusion is that the assumption of non-evolution of the orbit over the time-period that the debris explores is incorrect.

Since simulated debris in the region with troublesome velocities is cyan and green (lost 2 and 3 orbits ago respectively), we estimate the timescale over which the evolution has taken place to be $\sim 2-3$ Gyrs. We can get some idea of the physical scale of the evolution necessary by looking at the difference between the orbits in prolate, spherical and oblate potentials that is responsible for the difference in the velocity trend. Figure 13 plots the orbits shown in Figure 2 in Galactic coordinates with the region corresponding to the leading debris velocity data shown as bold along each curve.

As the potential moves from prolate to oblate, the orbit passes progressively nearer the Sun and line-of-sight velocities more closely reflect the full motion along the orbit. This explains why the simulated line of sight velocities in this region become more extreme with the oblateness of the potential. Figure 13 also suggests that observed debris velocities in the leading region might be accounted for even in an oblate or spherical potential if the pericenter of Sgr’s orbit has decreased by a factor of order unity within the last 2-3 Gyrs (from visual inspection of the figure) since such a decrease in pericenter of the Sgr *dwarf* over time could shift older Sgr *debris* out to greater distances from the Sun corresponding to the greater pericenter of the dwarf on the passage on which the debris became unbound. Three factors could contribute to this evolution:

An encounter with a large lump in the Milky Way potential, either dark or luminous (e.g. such as the Large Magellanic Cloud, see Zhao 1998, for a full description of this idea): We consider this unlikely since we would expect the signature of such an event to be a sudden change in Sgr’s orbit, and a corresponding sudden change in the velocities along its debris, rather than the smooth trends seen.

Global evolution of the Galactic potential: We also consider this unlikely since: (i) The evolution would have to be very large in order to bring the pericenter inwards by a factor of two in such a short amount of time; and (ii) any global evolution would affect both Sgr’s and the debris’ orbits similarly.

Dynamical friction: If we re-arrange equation [7-27] from Binney & Tremaine (1987) we can find the mass necessary M_{fric} for a circular orbit at $r = 30$ kpc (i.e. to represent an orbit with of order unity larger pericenter than Sgr today) to decay to the center of the Galaxy over a time period $t_{\text{fric}} = 2$ Gyrs in a Galaxy with a flat rotation curve and $v_{\text{circ},\odot} = 220$ km s⁻¹:

$$M_{\text{fric}} = \frac{1}{\ln \Lambda} \left(\frac{1.0 \times 10^{10} \text{Gyrs}}{t_{\text{fric}}} \right) \left(\frac{r}{60 \text{kpc}} \right)^2 \left(\frac{v_{\text{circ},\odot}}{220 \text{km s}^{-1}} \right) 2 \times 10^{10} M_{\odot}. \quad (7)$$

Binney & Tremaine (1987) estimate $\ln \Lambda \sim 3$ for the combined Large and Small Magellanic Clouds. Since we expect $\Lambda \propto 1/M_{\text{fric}}$, and know the current mass of Sgr to be $2 - 5 \times 10^8 M_{\odot}$, we expect $\ln \Lambda = 5 - 9$ to be the relevant range for our own estimate and hence $M_{\text{fric}} \sim 2.5 - 5 \times 10^9 M_{\odot}$. Moreover, we consider this only a lower limit on the necessary mass since Sgr’s orbit is not circular. (See Jiang & Binney 2000; Zhao 2004, for a general discussion of dynamical friction acting on Sgr over a Hubble time.)

Although dynamical friction seems like the most favourable explanation for the orbit evolution it does require Sgr to be an order of magnitude more massive just 2 Gyrs ago

and debris lost at that time in our mass-follows-light models would have a correspondingly larger dispersion in velocity (by a factor of order $\sqrt{10} = 3$) and distances. Since the observed velocity dispersion in the debris in the discrepant, leading portion of the stream is actually quite similar to that seen in our simulations ($\sim 17 \text{ km s}^{-1}$, see Fig. 10) this suggests that, in order to fit the data, in addition to dropping our assumption of a single orbit for Sgr, we will also have to move beyond modelling Sgr as a *single component* system. Hence, while the mean trend in the leading streamer will tell us how much total mass needs to have been lost from Sgr, the low dispersion offers the additional opportunity of constraining how much more tightly bound the light matter is compared to the dark matter. A study of these combined effects is in progress.

5. SUMMARY

In this paper we have presented the first model of the tidal tails of the Sgr dwarf galaxy based upon a coherent, all-sky picture of the system in both position and radial velocity, as represented by M giants selected from the 2MASS database. We summarize our conclusions as follows:

Shape and evolution of the Galactic potential — In a companion paper (Paper III) we have shown that *oblate* ($q = 0.90$) models of the Galactic halo potential best reproduce the difference in orbital poles between leading and trailing M giant tidal debris, while in this paper (see also Helmi (2004)) we find that *prolate* ($q = 1.25$) models are required to reproduce the trend of observed M giant leading debris velocities. Although we explore a wide variety of Galactic potentials we fail to find a single orbit that can simultaneously reproduce the observed orbital pole precession and leading debris velocity trend, and conclude that some evolution of the orbit of Sgr has occurred over the past few Gyr.

Mass of the Milky Way Galaxy — Within our simulations that best reproduce the observed Sgr dwarf tidal tails, the enclosed mass of the Milky Way within 50 kpc is found to be $3.8 - 5.6 \times 10^{11} M_{\odot}$.

Mass of the Sgr dwarf — The present bound mass of the Sgr dwarf has been restricted to the range $M_{\text{Sgr}} = 2 - 5 \times 10^8 M_{\odot}$, constrained by the width and velocity dispersion of the trailing M giant tidal tail. Taking $L_{\text{Sgr}} = 1.4 \times 10^7 L_{\odot}$ as the luminosity of Sgr, this gives a range of possible values for the mass-to-light ratio of Sgr from $M_{\text{Sgr}}/L_{\text{Sgr}} = 14 - 36$. Although all of our models maintained cores of bound material, we would expect similar dispersions to be seen in the debris if a similar amount of recently unbound

(i.e. on the current pericentric passage) mass were present within the same distance scale.

Orbit of Sgr — The Sgr orbit in our best-fit models ($q = 0.90/1.0/1.25$) has a pericenter of 10-16/14/14-19 kpc, an apocenter of 56-58/59/56-59 kpc and a radial time period of 0.85/0.88/0.87 Gyr. These values depend on the distance scale adopted for the M giants and the exact form of the Galactic potential.

Proper motion of Sgr — For our best-fit models ($q = 0.90/1.0/1.25$), the tidal tails of the dwarf as traced by 2MASS M giants are best reproduced by a satellite situated at $(X, Y, Z) = (16.2, 2.3, -5.9)$ kpc with velocity tangential to the line-of-sight $v_{\tan} = 275-280/265-270/255-260$ km s $^{-1}$ corresponding to space velocities $(U, V, W) = (238, -42, 222)/(235, -40, 213)/(231, -37, 198)$ km s $^{-1}$, i.e. $(\Pi, \Theta, Z) = (230, 75, 222)/(227, 73, 213)/(224, 69, 197)$ km s $^{-1}$, $(v_r, v_b, v_l) = (171, 272, -65)/(171, 263, -63)/(171, 247, -59)$ km s $^{-1}$, and proper motion $\mu_l \cos(b) = -2.59/-2.57/-2.54$ mas yr $^{-1}$ and $\mu_b = 2.26/2.18/2.05$ mas yr $^{-1}$ in the Solar rest frame. These velocities are dependent on the model assumed for the Galactic potential, and will scale roughly with choice of $v_{\text{circ},\odot}$ and other Galactic parameters.

Solar neighborhood debris — Our best-fit models orbiting in oblate ($q = 0.90$) and spherical ($q = 1.0$) potentials predict that the Sun is currently bathing in a stream of debris from Sgr, passing both inside and outside the Solar Circle. However, models orbiting in prolate ($q = 1.25$) potentials are inconsistent with this prediction, suggesting that conclusive proof of the presence or absence of Sgr debris in the Solar neighborhood could prove a useful tool for discriminating between models of the Galactic potential.

The authors would like to thank M.F. Skrutskie for helpful discussion, and D. Martínez-Delgado and M.A. Gómez-Flechoso for clarification on their satellite model and for making available a pre-publication copy of their latest work. SRM acknowledges support from Space Interferometry Mission Key Project NASA/JPL contract 1228235, NSF grant AST-0307851, a David and Lucile Packard Foundation Fellowship, and the F.H. Levinson Fund of the Peninsula Community Foundation. KVJ's contribution was supported through NASA grant NAG5-9064 and NSF CAREER award AST-0133617.

REFERENCES

- Binney, J. & Tremaine, S. 1987, Princeton, NJ, Princeton University Press, 1987, p. 429
- Edelsohn, D. J. & Elmegreen, B. G. 1997, MNRAS, 290, 7
- Eke, V. R., Navarro, J. F., & Steinmetz, M. 2001, ApJ, 554, 114
- Gómez-Flechoso, M. A., Fux, R., & Martinet, L. 1999, A&A, 347, 77
- Helmi, A. 2004, ApJ, 610L, 97
- Helmi, A. & White, S. D. M. 1999, MNRAS, 307, 495
- Helmi, A. & White, S.D.M. 2001, MNRAS, 323, 529
- Hernquist, L. & Ostriker, J.P. 1992, ApJ, 386, 375
- Ibata, R. A., Gilmore, G. & Irwin, M. J. 1995, MNRAS, 277, 781
- Ibata, R. A., Gilmore, G., & Irwin, M. J. 1994, Nature, 370, 194
- Ibata, R. A. & Lewis, G. F. 1998, ApJ, 500, 575
- Ibata, R.A., Lewis, G. F., Irwin, M.J., Totten, E., & Quinn, T 2001, ApJ, 551, 294
- Ibata, R. A., Wyse, R. F. G., Gilmore, G., Irwin, M. J., & Suntzeff, N. B. 1997, AJ, 113, 634
- Jiang, I. & Binney, J. 2000, MNRAS, 314, 468
- Jing, Y. P. & Suto, Y. 2002, ApJ, 574, 538
- Johnston, K.V. 1998, ApJ, 495, 297
- Johnston, K. V., Hernquist, L., & Bolte, M. 1996, ApJ, 465, 278
- Johnston, K. V., Law, D. R. & Majewski, S. R. 2004, ApJ submitted, astro-ph/0407565 (“Paper III”)
- Johnston, K. V., Majewski, S. R., Siegel, M. H., Reid, I. N., & Kunkel, W. E. 1999, AJ, 118, 1719
- Johnston, K. V., Sackett, P. B., & Bullock, J. S. 2001, ApJ, 557, 137
- Johnston, K. V., Spergel, D. N., & Hernquist, L. 1995, ApJ, 451, 598

- Kundu, A., Majewski, S.R., Rhee, J., Rocha-Pinto, H.J., Polak, A.A., Slesnick, C.L., Kunkel, W.E., Johnston, K.V., Patterson, R.J., Geisler, D., Gieren, W., Seguel, J., Smith, V.V., Palma, C., Arenas, J., Crane, J.D., & Hummels, C.B. 2002, ApJ, 576, 125
- Law, D. R., Majewski, S. R., Johnston, K. V., & Skrutskie, M. F. 2004, in Satellites and Tidal Streams, eds. F. Prada, D. Martinez-Delgado, T. Mahoney, ASP Conf. Ser., *in press* (astro-ph/0309567)
- Majewski, S.R. et al. 2004b, in preparation (“Paper V”)
- Majewski, S. R., Kunkel, W.E., Law, D.R., Polak, A.A., Rocha-Pinto, H.J., Crane, J.D., Frinchaboy, P.M., Hummels, C.B., Johnston, K.V., Patterson, R.J., Rhee, J., Skrutskie, M.F. & Weinberg, M.D. 2004a, AJ, 128, 245
- Majewski, S. R., Siegel, M. H., Kunkel, W. E., Reid, I. N., Johnston, K. V., Thompson, I. B., Landolt, A. U., & Palma, C. 1999, AJ, 118, 1709
- Majewski, S. R., Skrutskie, M.F., Weinberg, M.D. & Ostheimer, J.C. 2003, ApJ, 599, 1082 (“Paper I”)
- Martínez-Delgado, D., Gómez-Flechoso, M. Á., Aparicio, A., & Carrera, R. 2004, ApJ, 601, 242
- Mateo, M., Olszewski, E. W., & Morrison, H. L. 1998, ApJ, 508, L55
- Miyamoto, M. & Nagai, R. 1975, PASJ, 27, 533
- Monaco, L., Bellazzini, M., Ferraro, F. R., & Pancino, E. 2004, astro-ph/0406350
- Navarro, J. F., Frenk, C. S., & White, S. D. M. 1996, ApJ, 462, 563
- Newberg, H. J. et al. 2003, ApJ, 596, L191
- Plummer, H.C. 1911, MNRAS, 71, 460
- Totten, E.J. & Irwin, M.J. 1998, MNRAS, 294, 1
- Tremaine, S. 1993, AIP Conf. Proc. 278: Back to the Galaxy, 599
- Velazquez, H. & White, S. D. M. 1995, MNRAS, 275, 23
- Zhao, H. 1998, ApJ, 500, L149
- Zhao, H. 2004, MNRAS, 351, 891

Parameter/Property	Description	Value(s) tested	Constrained ^a by:	acceptable values ^b	value adopted
<i>Galactic parameters</i>					
d	scale length of the Galactic halo	0 - 20 kpc	4,5	1 - 20 kpc	13/12/11 kpc
q	flattening of the Galactic dark halo potential	0.8 - 1.4	6,7	0.8 - 1.4	0.90/1.0/1.25
$v_{\text{circ},\odot}$	circular velocity at R_{\odot}	180 - 240 km s ⁻¹	4,5	180 - 240 km s ⁻¹	220 km s ⁻¹
α	contribution of disk to rotation curve	0.25 - 1.00	4,5	0.25 - 1.00	1.00
<i>Kinematical parameters</i>					
v_{\tan}	tangential velocity of Sgr	200 - 400 km s ⁻¹	3,4,5,7	230 - 330 km s ⁻¹	280/270/254 km s ⁻¹
$v_{\text{los},\text{Sgr}}$	Sgr line of sight velocity	fixed	2	171 ± 1 km s ⁻¹	171 km s ⁻¹
<i>Positional parameters</i>					
D_{Sgr}	distance of Sgr from the Sun	22 - 28 kpc	4,5	22 - 28 kpc	24 kpc
$(l,b)_{\text{Sgr}}$	Galactic longitude and latitude of the Sgr dwarf	fixed	1	—	$(5.6^\circ, -14.2^\circ)$
R_{\odot}	distance of the Sun from the Galactic center	7.0 - 9.0 kpc	4,5	7.0 - 9.0 kpc	7.0 kpc
<i>Sagittarius dwarf parameters</i>					
M_{Sgr}	present bound mass of the Sgr dwarf ^c	$6 \times 10^6 - 3 \times 10^9 M_{\odot}$	8,9,10,11	$2 - 5 \times 10^8 M_{\odot}$	$4 \times 10^8 M_{\odot}$

Table 1: Parameter space of Milky Way - Sgr models considered, values quoted are for each of three models of the Galactic potential ($q = 0.90/1.0/1.25$ respectively). Comments — *a.*: See §2.2. *b.*: Acceptable ranges of values are considerably smaller once fixed parameters are adopted. *c.*: See Table 2 for further details.

Halo model	Constraint	Best-fit mass	Acceptable mass range
$q = 0.90$	σ_v	$2.3 \times 10^8 M_\odot$	$6.2 \times 10^7 M_\odot - 5.0 \times 10^8 M_\odot$
	$\sigma_{Z_{Sgr,\odot}}$	$3.8 \times 10^8 M_\odot$	$2.6 \times 10^8 M_\odot - 5.3 \times 10^8 M_\odot$
$q = 1.0$	σ_v	$2.8 \times 10^8 M_\odot$	$9.1 \times 10^7 M_\odot - 5.3 \times 10^8 M_\odot$
	$\sigma_{Z_{Sgr,\odot}}$	$3.7 \times 10^8 M_\odot$	$2.5 \times 10^8 M_\odot - 5.4 \times 10^8 M_\odot$
$q = 1.25$	σ_v	$4.8 \times 10^8 M_\odot$	$1.7 \times 10^8 M_\odot - 8.6 \times 10^8 M_\odot$
	$\sigma_{Z_{Sgr,\odot}}$	$3.8 \times 10^8 M_\odot$	$2.5 \times 10^8 M_\odot - 5.5 \times 10^8 M_\odot$

Table 2: Acceptable values for the present-day bound mass of the Sgr dwarf (M_{Sgr}) in each of our three halo models.

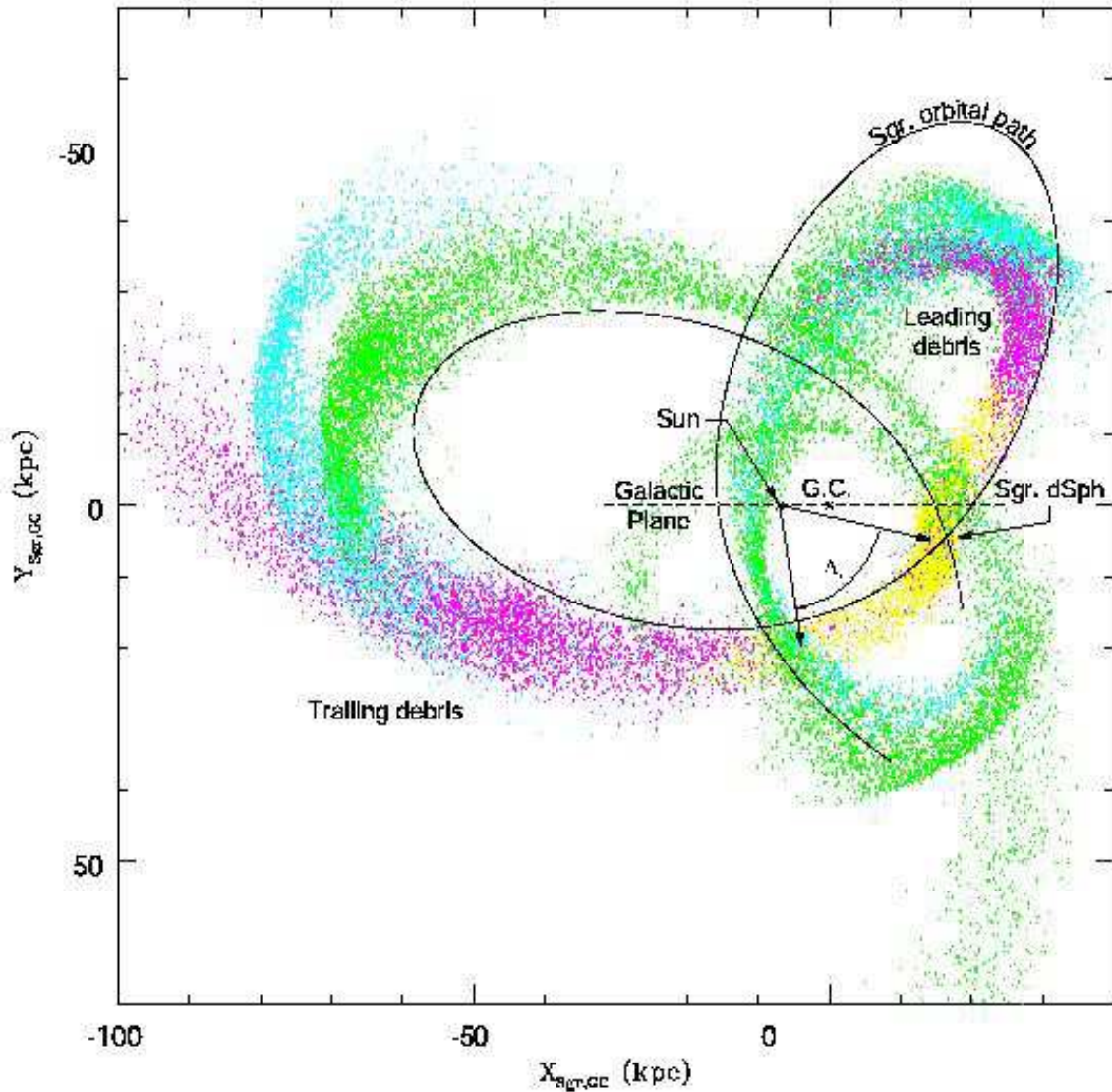


Fig. 1.— Typical appearance of an N-body tidal debris model (colored points) in the Sgr,GC plane (this corresponding to the best fit $q = 1.0$ model discussed later in §3.2.3). Each color corresponds to debris lost during a single radial orbit, and the solid line is the projected orbit of the Sgr dwarf core. Bold arrows define the longitudinal coordinate system adopted throughout this paper.

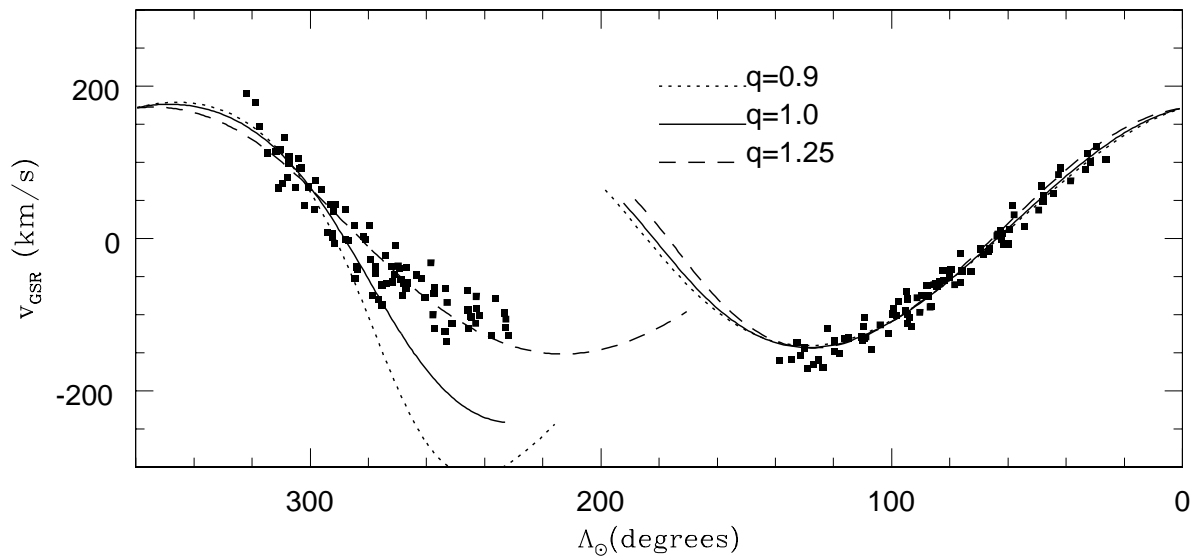


Fig. 2.— Square points show the selected velocity data in leading and trailing arms that represent the general trend and dispersion of Sgr debris in these regions. Solid/dashed/dotted curves show “best” (as defined in §3.1.3) orbits selected to fit the trailing data alone in the final potentials adopted with the specified q in §3.1.5C

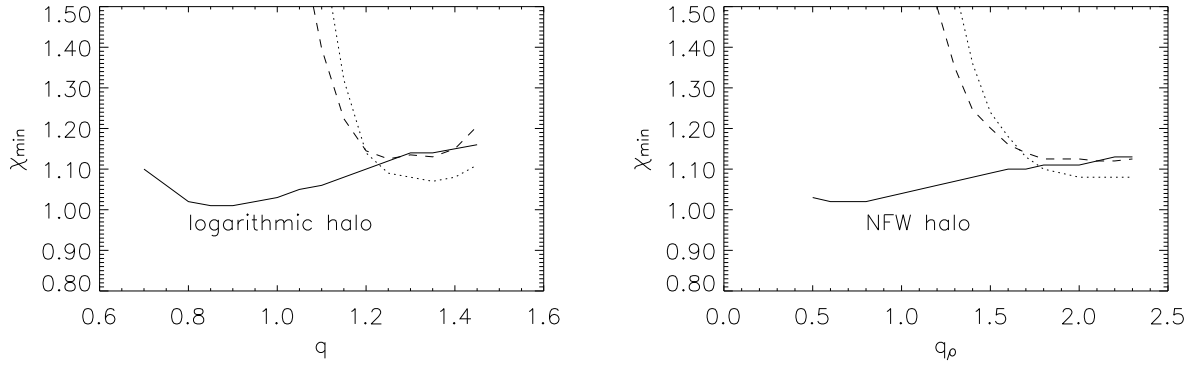


Fig. 3.— Minimum values of χ_{trail} (solid lines, equation 5), χ_{lead} (dotted lines, equation 5) and χ (dashed lines, equation 6) as a function of q (in potentials with logarithmic halo components — left hand panel) or q_ρ (in potentials with NFW halo component — right hand panel) when all other parameters are varied freely.

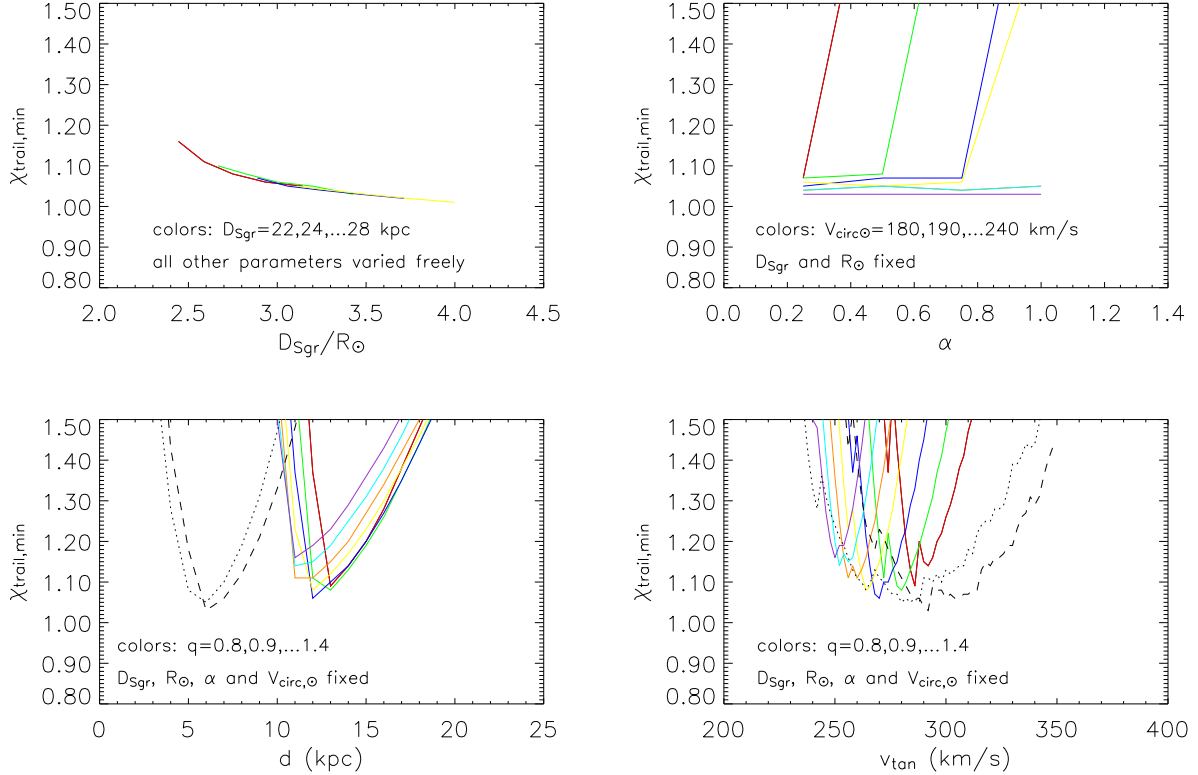


Fig. 4.— Projections of results in our 7-dimensional parameter space onto two-dimensions for experiments with logarithmic halo components. One axis of the plane is plotted along the x -axis and the other represented by the different colored lines — the upper label in each panel gives the second dimension explored with the numbers corresponding in sequence to red/green/blue/yellow/orange/light blue/violet lines. (Note: in some panels certain colors appear to be missing in the sequence because the lines are overplotted on top of one another.) The y -axis shows the minimum χ_{trail} in the illustrated plane when: (i) *upper left hand panel* — all other parameters vary freely; (ii) *upper right hand panel* — $D_{\text{Sgr}} = 24$ kpc and $R_{\odot} = 7$ kpc and (iii) *lower panels* — $D_{\text{Sgr}} = 24$ kpc, $R_{\odot} = 7$ kpc, $v_{\text{circ},\odot} = 220$ km s^{-1} and $\alpha = 1$. Dashed black curves in the lower panels outline where colored curves would fall with same fixed parameters but $v_{\text{circ},\odot} = 240$ km s^{-1} . Dotted black curves outline the location for $v_{\text{circ},\odot} = 220$ km s^{-1} and $\alpha = 0.5$.

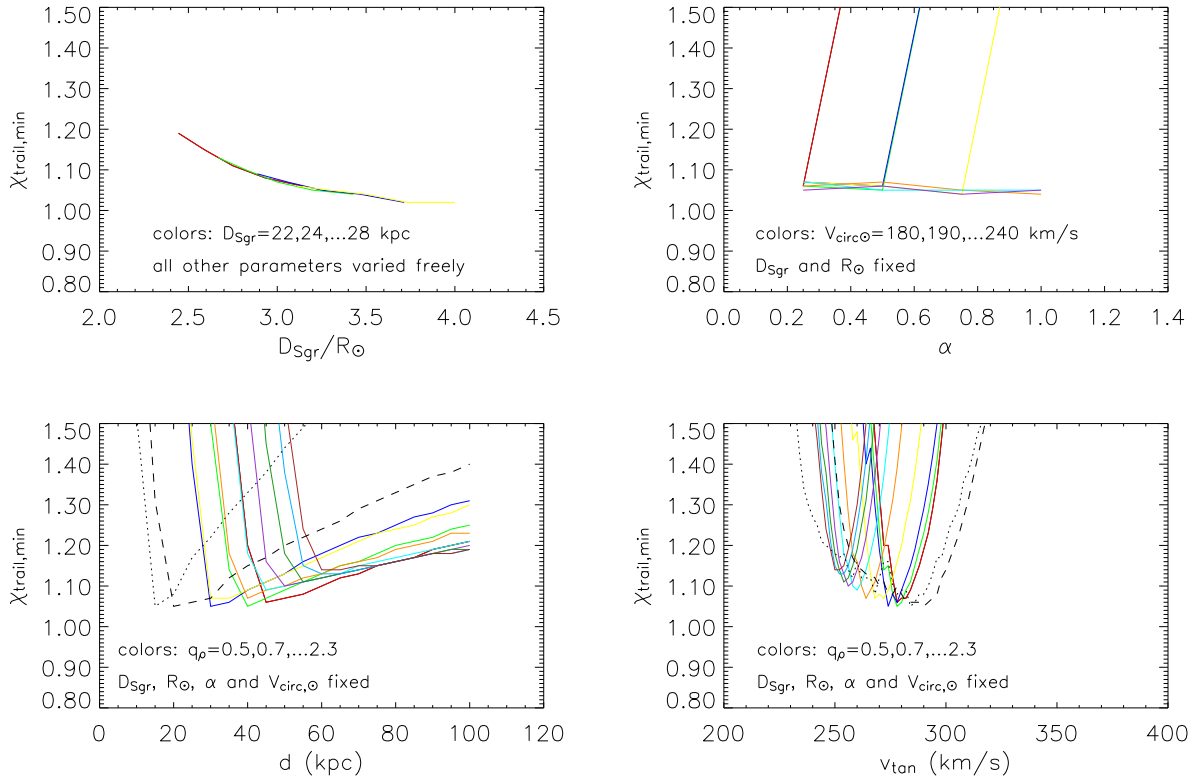


Fig. 5.— As Figure 4 but for models with NFW halo components. In this case $v_{\text{circ},\odot}$ is held fixed at 230 km s⁻¹ in the colored and dotted black lines in the lower panels. All other fixed quantities in the lower panels are the same.

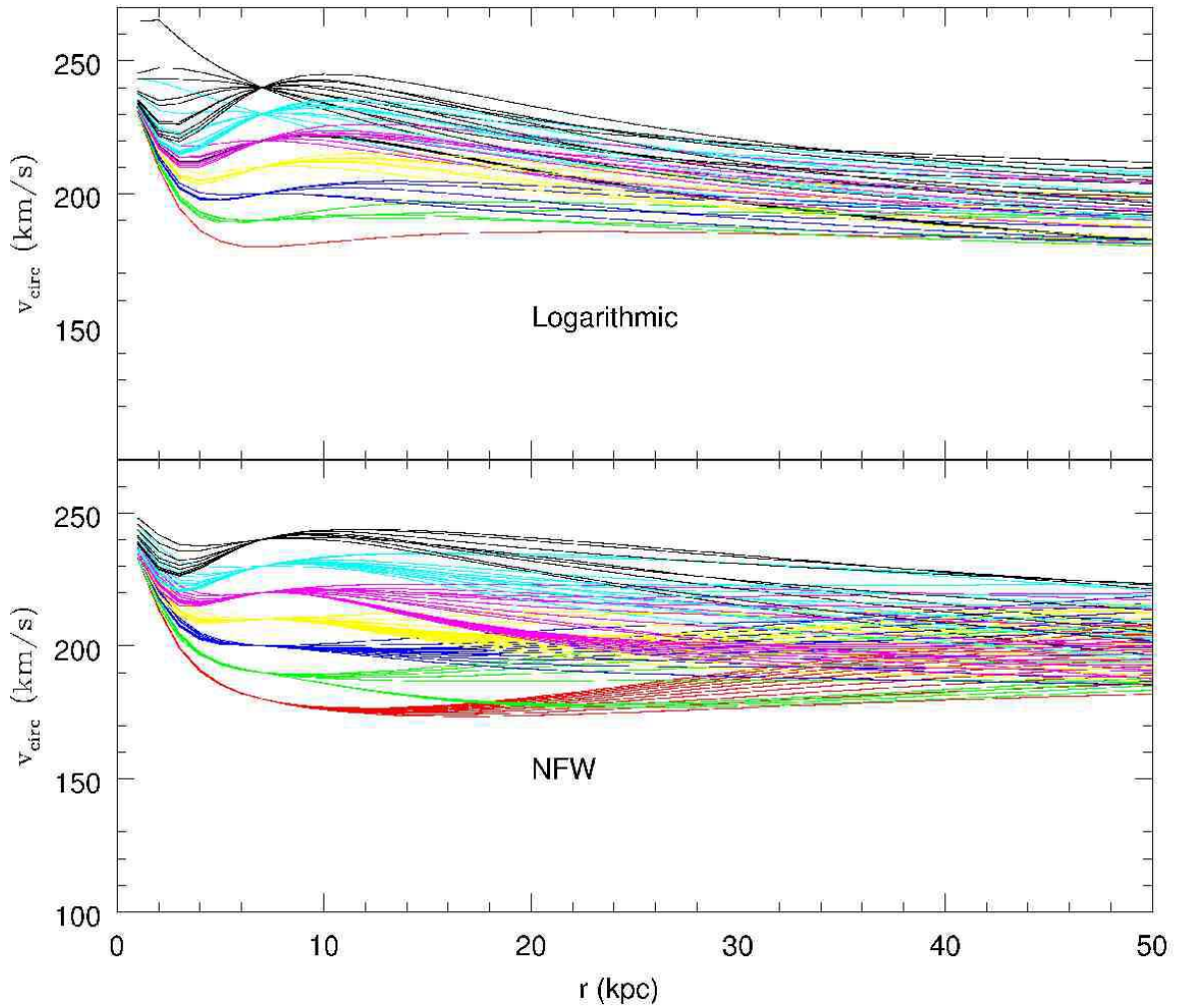


Fig. 6.— Rotation curves for all models with logarithmic (upper panel) or NFW (lower panel) halo components in which orbits can be found that satisfy both $1 < D_{\text{max}}/D_{\text{debris}} < 1.5$ and $\chi_{\text{trail}} < 1.1$. Colors black/cyan/magenta/yellow/blue/green/red correspond to potentials with $v_{\text{circ},\odot} = 240/230/220/210/200/190/180$ km s $^{-1}$ at $R_{\odot} = 7$ kpc.

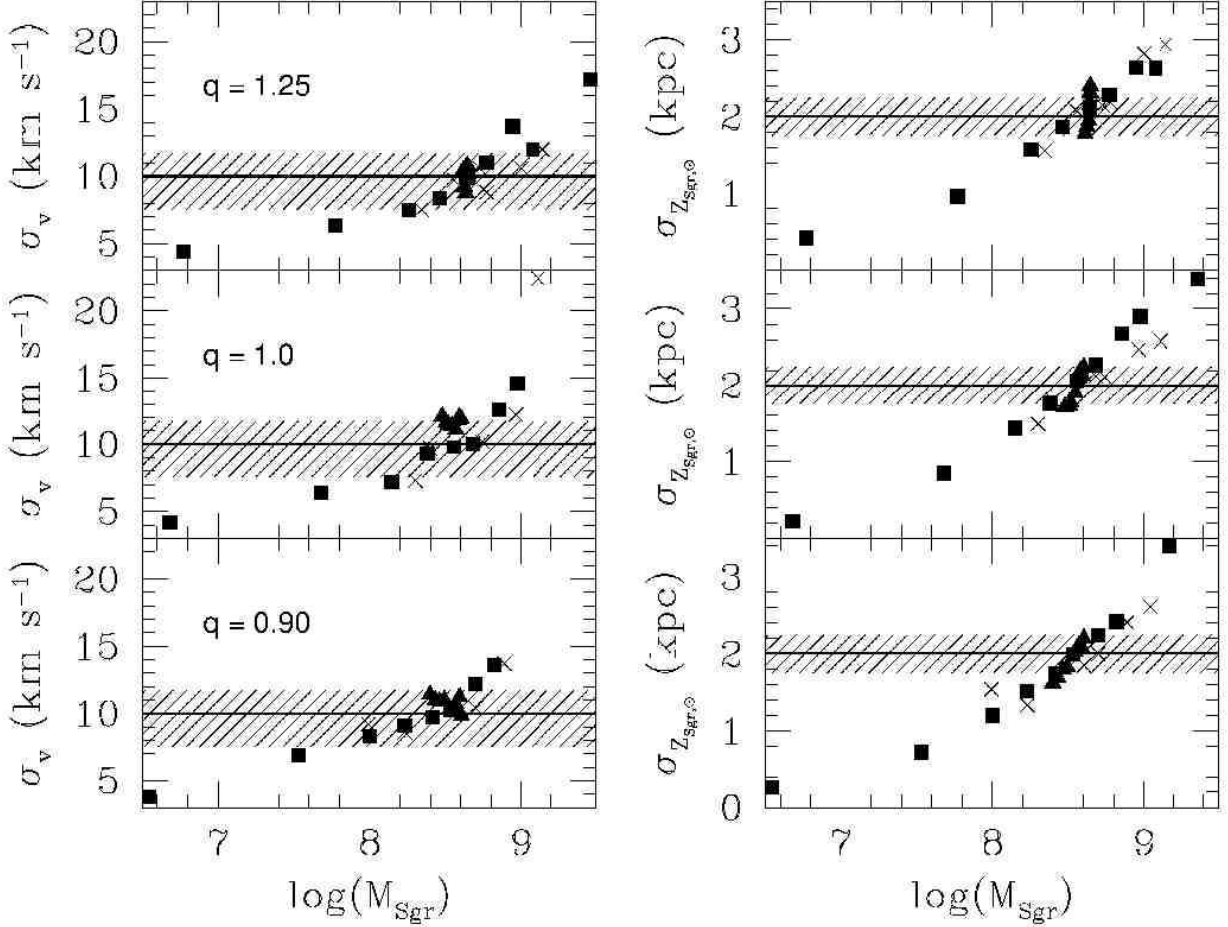


Fig. 7.— The velocity dispersion of trailing satellite debris (σ_v) and spatial dispersion of trailing debris perpendicular to the Sgr plane ($\sigma_{Z_{\text{Sgr},\infty}}$) are plotted as functions of present satellite mass M_{Sgr} for oblate ($q = 0.90$, bottom row), spherical ($q = 1.0$, middle row), and prolate ($q = 1.25$, top row) models of the Galactic halo potential. The solid lines represent the fiducial values found for 2MASS M giants from Papers I and II, and the hatched areas show the regions that are within one standard deviation of these measurements. Square points are for a series of simulations along a given orbit ($v_{\text{tan}} = 280/270/254 \text{ km s}^{-1}$ for $q = 0.90/1.0/1.25$ respectively) but with initial dwarf mass and scale length pairs chosen to produce a similar central density. Crosses represent simulations along these same orbits and in a similar initial mass range for the dwarf but with a variety of scale lengths, and triangles represent simulations with fixed initial mass and scale length evolved along orbits with v_{tan} in the range $\pm 20 \text{ km s}^{-1}$ around $280/270/254 \text{ km s}^{-1}$.

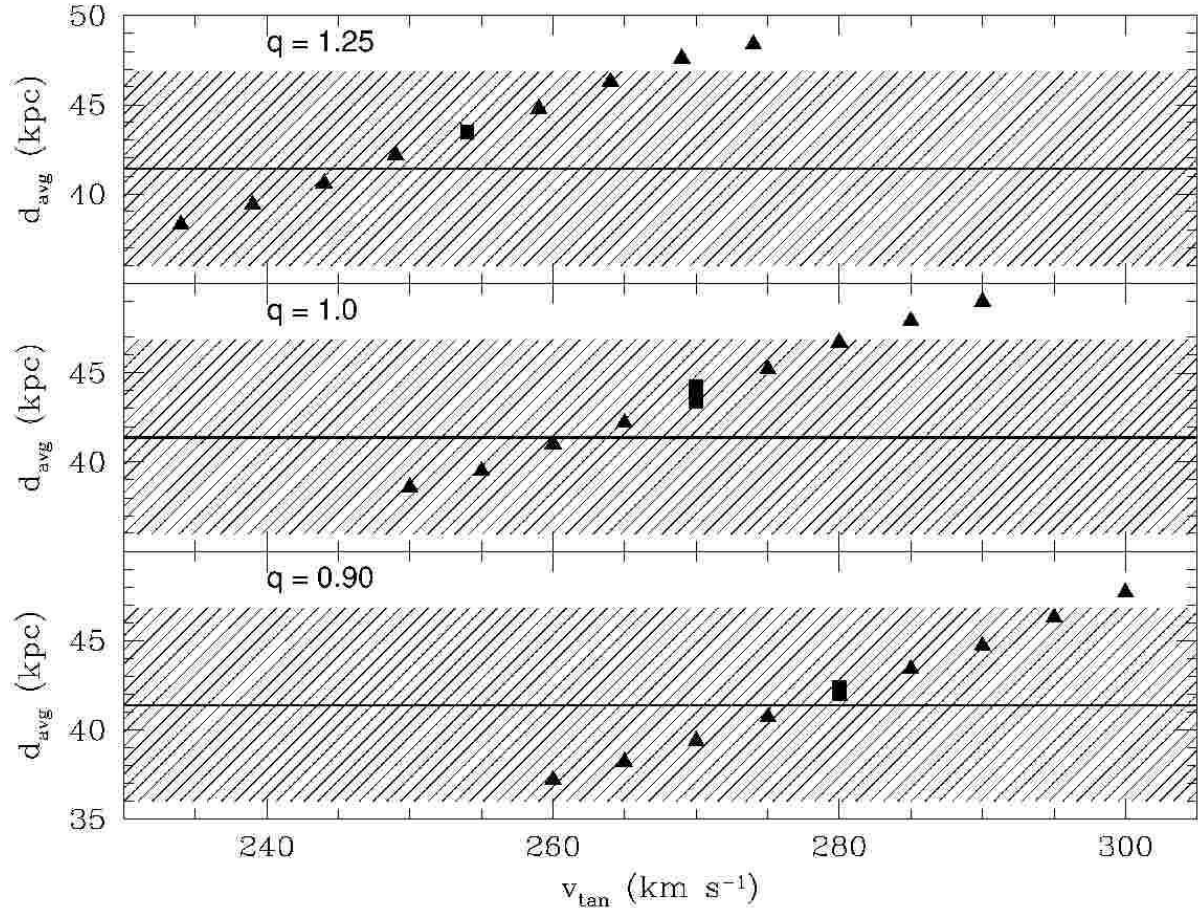


Fig. 8.— Average distance of leading apoGalacticon debris (d_{avg}), plotted as a function of the tangential velocity parameter v_{tan} for oblate ($q = 0.90$, bottom panel), spherical ($q = 1.0$, middle panel), and prolate ($q = 1.25$, top panel) models of the Galactic halo potential. The solid lines represent the fiducial values found for 2MASS M giants from Paper I, and the hatched areas show the regions that are within one standard deviation of those measurements. Symbols are the same as in Figure 7, but only those square points and crosses which fall within the hatched regions on Figure 7 are included here.

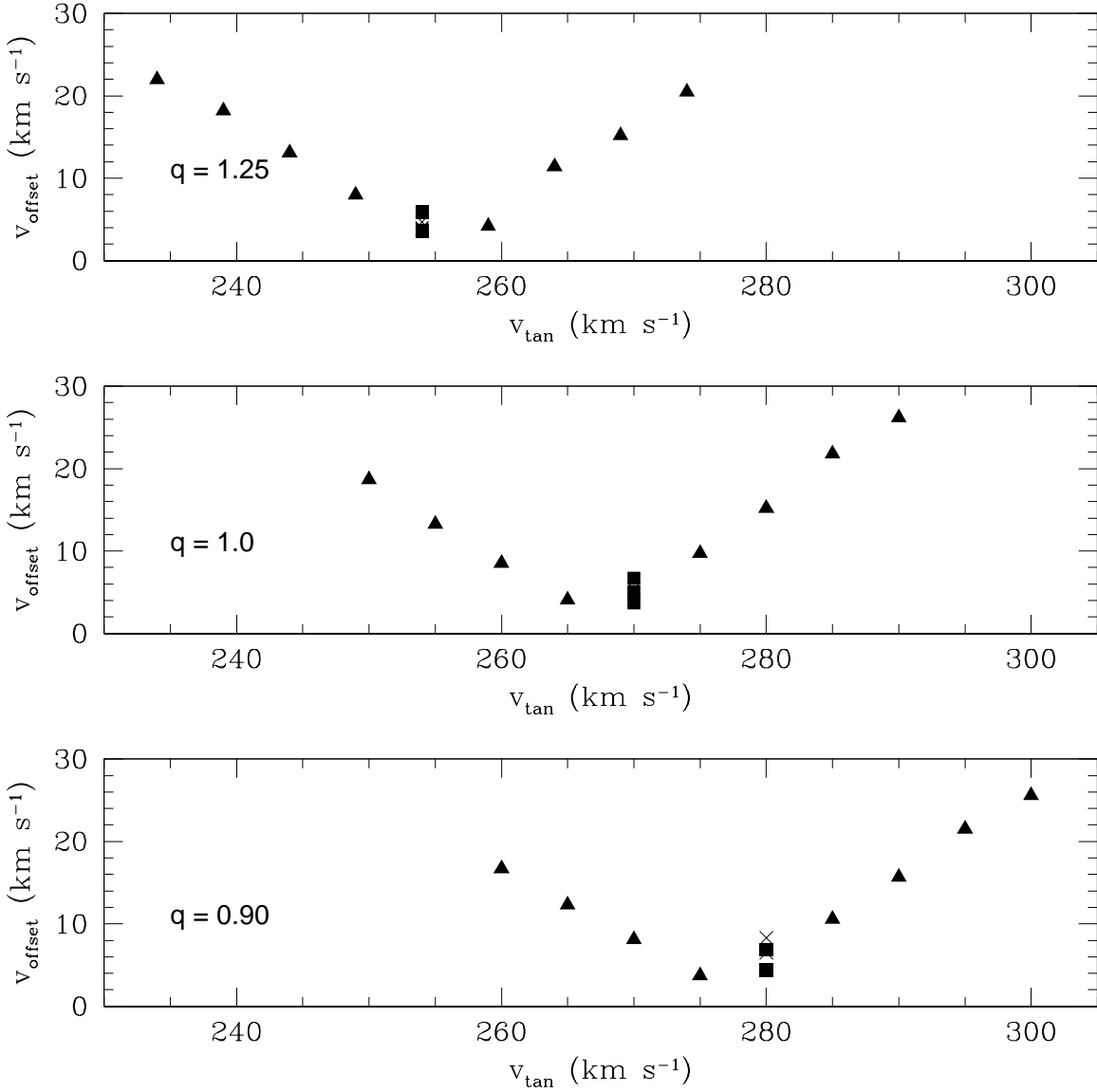


Fig. 9.— Average offset of trailing debris velocities from the fiducial Sgr stream velocities (Paper II) for a range of choices of the model Sgr dwarf velocity v_{tan} in oblate ($q = 0.90$, bottom row), spherical ($q = 1.0$, middle row), and prolate ($q = 1.25$, top row) models of the Galactic halo potential. Symbols are the same as in Figure 7, but only those square points and crosses which fall within the hatched regions on Figure 7 are included here.

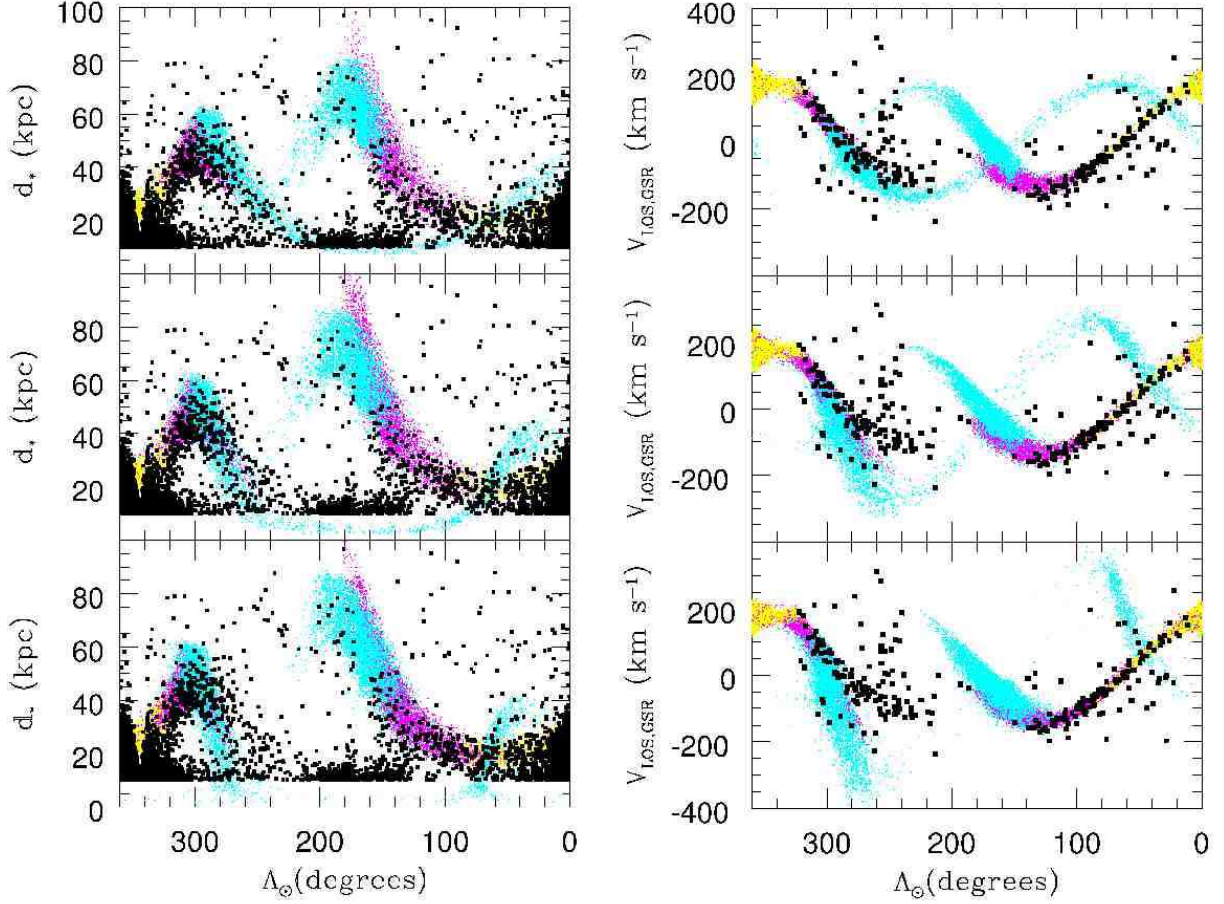


Fig. 10.— Distance and velocity data are plotted as a function of orbital longitude for simulated satellite debris from the best-fit models in oblate ($q = 0.90$, bottom row), spherical ($q = 1.0$, middle row), and prolate ($q = 1.25$, top row) models of the Galactic halo potential (colored points) and 2MASS M giant data from Papers I, II, and V (black points and solid squares, compare to Figs. 10 and 6 of Papers I and II respectively). A 17% artificial random distance scatter has been applied to simulated debris particles to mimic the photometric distance error present in the 2MASS sample. Note that M giants closer than 10 kpc have been omitted from the lower panel in order to show nearby simulated debris.

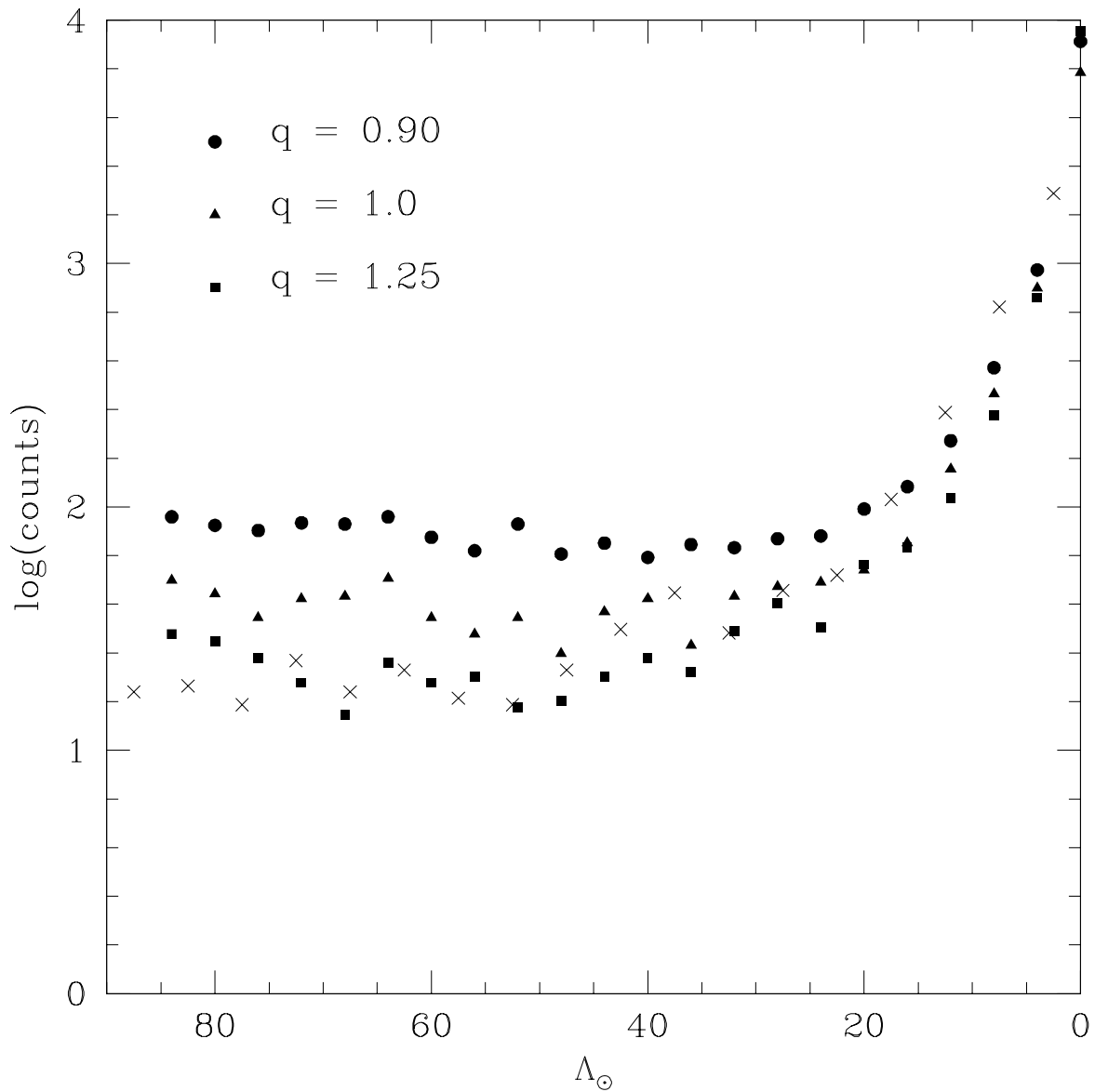


Fig. 11.— Counts (per 4° of orbital longitude) of debris along the trailing tail, data are shown for the best-fit models (filled circles/triangles/squares) and for background-subtracted M giant data (crosses) from Paper I.

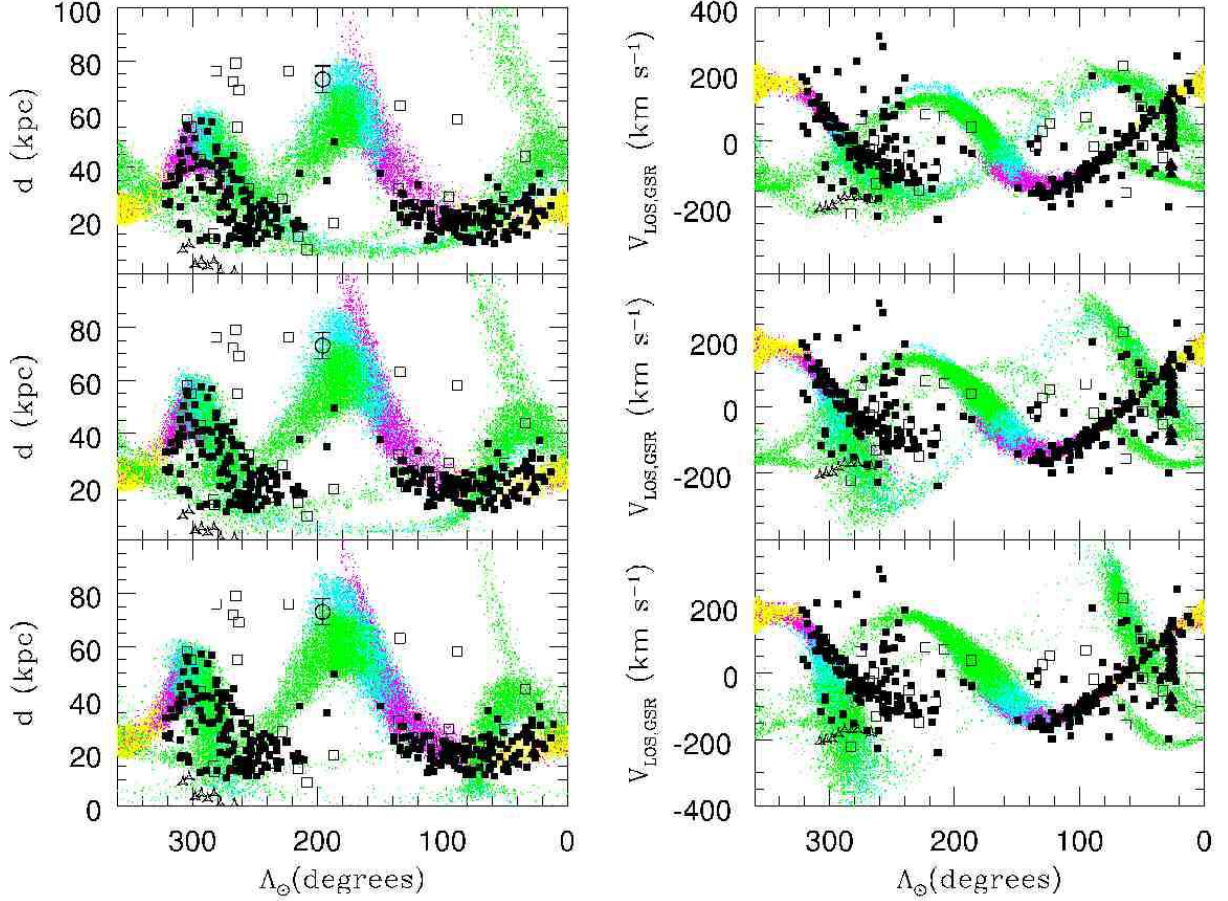


Fig. 12.— Distances and radial velocities of debris from the best-fit models in oblate ($q = 0.90$, bottom row), spherical ($q = 1.0$, middle row), and prolate ($q = 1.25$, top row) models of the Galactic halo potential (colored points) are overplotted with data from selected recent observations. Filled squares denote data from Papers II and V, open boxes represent carbon stars selected from Totten & Irwin (1998), solid triangles are data from Majewski et al. (1999), open triangles are data from Kundu et al. (2002), and the open circle is from Newberg et al. (2003). A 17% artificial random distance scatter has been applied to simulated debris particles to mimic the photometric distance error present in the 2MASS sample.

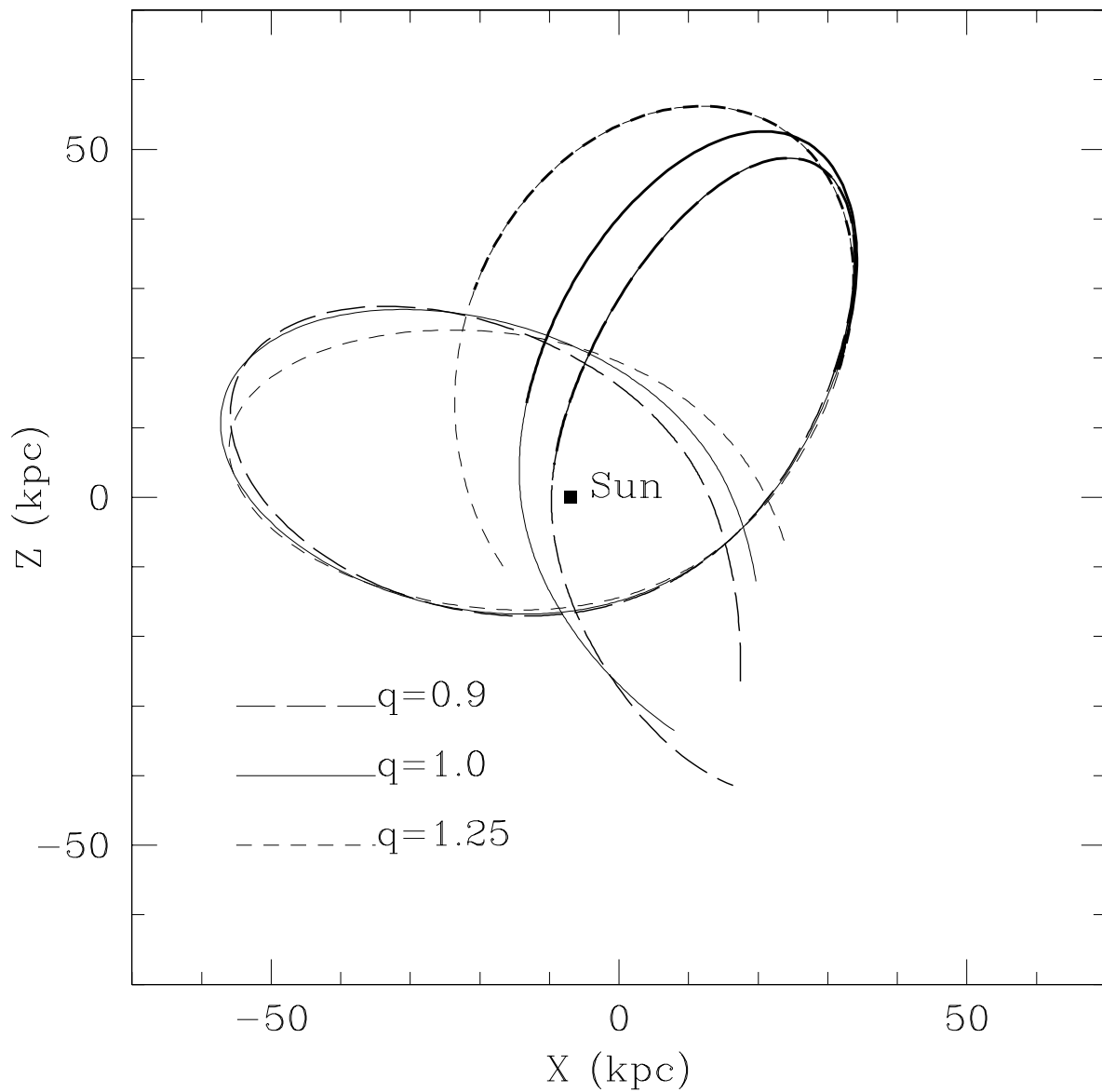


Fig. 13.— Plots in Galactic coordinates of the same orbits shown in Figure 2.